THE *NuSTAR* EXTRAGALACTIC SURVEY: A FIRST SENSITIVE LOOK AT THE HIGH-ENERGY COSMIC X-RAY BACKGROUND POPULATION

D. M. ALEXANDER[1], D. STERN[2], A. DEL MORO[1], G. B. LANSBURY[1], R. J. ASSEF[2,23], J. AIRD[1], M. AJELLO[3], D. R. BALLANTYNE[4],
F. E. BAUER[5,6], S. E. BOGGS[3], W. N. BRANDT[7,8], F. E. CHRISTENSEN[9], F. CIVANO[10,11], A. COMASTRI[12], W. W. CRAIG[9,13],
M. ELVIS[11], B. W. GREFENSTETTE[14], C. J. HAILEY[15], F. A. HARRISON[14], R. C. HICKOX[10], B. LUO[7,8], K. K. MADSEN[14],
J. R. MULLANEY[1], M. PERRI[16,17], S. PUCCETTI[16,17], C. SAEZ[5], E. TREISTER[18], C. M. URRY[19], W. W. ZHANG[20], C. R. BRIDGE[21],
P. R. M. EISENHARDT[2], A. H. GONZALEZ[22], S. H. MILLER[21], AND C. W. TSAI[2]

[1] Department of Physics, Durham University, Durham DH1 3LE, UK
[2] Jet Propulsion Laboratory, California Institute of Technology, 4800 Oak Grove Drive, Mail Stop 169-221, Pasadena, CA 91109, USA
[3] Space Sciences Laboratory, University of California, Berkeley, CA 94720, USA
[4] Center for Relativistic Astrophysics, School of Physics, Georgia Institute of Technology, Atlanta, GA 30332, USA
[5] Departamento de Astronomía y Astrofísica, Pontificia Universidad Católica de Chile, Casilla 306, Santiago 22, Chile
[6] Space Science Institute, 4750 Walnut Street, Suite 205, Boulder, CO 80301, USA
[7] Department of Astronomy and Astrophysics, 525 Davey Lab, The Pennsylvania State University, University Park, PA 16802, USA
[8] Institute for Gravitation and the Cosmos, The Pennsylvania State University, University Park, PA 16802, USA
[9] DTU Space–National Space Institute, Technical University of Denmark, Elektrovej 327, DK-2800 Lyngby, Denmark
[10] Department of Physics and Astronomy, Dartmouth College, 6127 Wilder Laboratory, Hanover, NH 03755, USA
[11] Harvard-Smithsonian Center for Astrophysics, 60 Garden Street, Cambridge, MA 02138, USA
[12] INAF–Osservatorio Astronomico di Bologna, Via Ranzani 1, I-40127 Bologna, Italy
[13] Lawrence Livermore National Laboratory, Livermore, CA 94550, USA
[14] Cahill Center for Astrophysics, 1216 East California Boulevard, California Institute of Technology, Pasadena, CA 91125, USA
[15] Columbia Astrophysics Laboratory, 550 W 120th Street, Columbia University, NY 10027, USA
[16] ASI–Science Data Center, via Galileo Galilei, I-00044 Frascati, Italy
[17] INAF–Osservatorio Astronomico di Roma, via Frascati 33, I-00040 Monteporzio Catone, Italy
[18] Departamento de Astronomía, Universidad de Concepción, Casilla 160-C, Concepción, Chile
[19] Yale Center for Astronomy and Astrophysics, Physics Department, Yale University, P.O. Box 208120, New Haven, CT 06520-8120, USA
[20] NASA Goddard Space Flight Center, Greenbelt, MD 20771, USA
[21] California Institute of Technology, MS249-17, Pasadena, CA 91125, USA
[22] Department of Astronomy, University of Florida, Gainesville, FL 32611-2055, USA

ABSTRACT

We report on the first 10 identifications of sources serendipitously detected by the *Nuclear Spectroscopic Telescope Array* (*NuSTAR*) to provide the first sensitive census of the cosmic X-ray background source population at $\gtrsim 10$ keV. We find that these *NuSTAR*-detected sources are ≈ 100 times fainter than those previously detected at $\gtrsim 10$ keV and have a broad range in redshift and luminosity ($z = 0.020$–2.923 and $L_{10-40\,\mathrm{keV}} \approx 4 \times 10^{41}$–$5 \times 10^{45}$ erg s^{-1}); the median redshift and luminosity are $z \approx 0.7$ and $L_{10-40\,\mathrm{keV}} \approx 3 \times 10^{44}$ erg s^{-1}, respectively. We characterize these sources on the basis of broad-band ≈ 0.5–32 keV spectroscopy, optical spectroscopy, and broad-band ultraviolet-to-mid-infrared spectral energy distribution analyses. We find that the dominant source population is quasars with $L_{10-40\,\mathrm{keV}} > 10^{44}$ erg s^{-1}, of which $\approx 50\%$ are obscured with $N_{\mathrm{H}} \gtrsim 10^{22}$ cm^{-2}. However, none of the 10 *NuSTAR* sources are Compton thick ($N_{\mathrm{H}} \gtrsim 10^{24}$ cm^{-2}) and we place a 90% confidence upper limit on the fraction of Compton-thick quasars ($L_{10-40\,\mathrm{keV}} > 10^{44}$ erg s^{-1}) selected at $\gtrsim 10$ keV of $\lesssim 33\%$ over the redshift range $z = 0.5$–1.1. We jointly fitted the rest-frame ≈ 10–40 keV data for all of the non-beamed sources with $L_{10-40\,\mathrm{keV}} > 10^{43}$ erg s^{-1} to constrain the average strength of reflection; we find $R < 1.4$ for $\Gamma = 1.8$, broadly consistent with that found for local active galactic nuclei (AGNs) observed at $\gtrsim 10$ keV. We also constrain the host-galaxy masses and find a median stellar mass of $\approx 10^{11}\,M_{\odot}$, a factor ≈ 5 times higher than the median stellar mass of nearby high-energy selected AGNs, which may be at least partially driven by the order of magnitude higher X-ray luminosities of the *NuSTAR* sources. Within the low source-statistic limitations of our study, our results suggest that the overall properties of the *NuSTAR* sources are broadly similar to those of nearby high-energy selected AGNs but scaled up in luminosity and mass.

Key words: galaxies: active – galaxies: high-redshift – infrared: galaxies – X-rays: diffuse background – X-rays: general

Online-only material: color figures

1. INTRODUCTION

The cosmic X-ray background (CXB) was first discovered in the early 1960s (Giacconi et al. 1962), several years before the detection of the cosmic microwave background (CMB; Penzias & Wilson 1965). However, unlike the CMB, which is truly diffuse in origin, the CXB is dominated by the emission from high-energy distant point sources: active galactic nuclei (AGNs), the sites of intense black-hole growth that reside at the centers of galaxies (see Brandt & Hasinger 2005; Brandt & Alexander 2010 for reviews). A key goal of high-energy astrophysics is to determine the detailed composition of the CXB in order to understand the evolution of AGNs.

Huge strides in revealing the composition of the CXB have been made over the past decade, with sensitive surveys

---

[23] NASA Postdoctoral Program Fellow.

undertaken by the *Chandra* and *XMM-Newton* observatories (e.g., Alexander et al. 2003a; Hasinger et al. 2007; Brunner et al. 2008; Luo et al. 2008; Comastri et al. 2011; Xue et al. 2011). These surveys are so deep that they have resolved ≈70%–90% of the CXB at energies of ≈0.5–8 keV (e.g., Worsley et al. 2005; Hickox & Markevitch 2006; Lehmer et al. 2012; Xue et al. 2012), revealing a plethora of obscured and unobscured AGNs out to $z \approx$ 5–6. However, although revolutionary, *Chandra* and *XMM-Newton* are only sensitive to sources detected at ≈0.5–10 keV, far from the peak of the CXB at ≈20–30 keV (e.g., Frontera et al. 2007; Ajello et al. 2008; Moretti et al. 2009; Ballantyne et al. 2011). Until recently, the most powerful observatories with sensitivity at ≈20–30 keV have only resolved ≈1%–2% of the CXB at these energies (e.g., Krivonos et al. 2007; Ajello et al. 2008, 2012; Bottacini et al. 2012) and therefore provide a limited view of the dominant source populations (e.g., Sazonov & Revnivtsev 2004; Markwardt et al. 2005; Bassani et al. 2006; Treister et al. 2009b; Bird et al. 2010; Tueller et al. 2010; Burlon et al. 2011).

A great breakthrough in resolving the peak of the CXB is the *Nuclear Spectroscopic Telescope Array* (*NuSTAR*) observatory. *NuSTAR* was successfully launched on 2012 June 13 and is the first >10 keV orbiting observatory with focusing optics (Harrison et al. 2013). *NuSTAR*'s focusing optics provide a ≈1 order of magnitude improvement in angular resolution and a ≈2 orders of magnitude improvement in sensitivity over previous-generation >10 keV observatories, a revolutionary leap forward in performance. One of the primary objectives of *NuSTAR* is to complete a sensitive extragalactic survey and identify the source populations that produce the peak of the CXB.

The *NuSTAR* extragalactic survey comprises three components (see Table 6 of Harrison et al. 2013): a deep small-area survey in the Extended Chandra Deep Field-South (E-CDF-S; Lehmer et al. 2005) field, a medium wider-area survey in the Cosmic Evolution Survey (COSMOS; Scoville et al. 2007) field, and a large area (typically shallow) serendipitous survey conducted in the fields of other *NuSTAR* targets, including ≈100 *Swift*-BAT identified AGNs. In this paper we report on the first 10 spectroscopically identified sources in the *NuSTAR* serendipitous survey. In Section 2 we present the *NuSTAR* observations of the serendipitous sources, the multi-wavelength data, and the details of our data processing approaches, in Section 3 we describe our analysis of the X-ray and multi-wavelength data, in Section 4 we present our results, and in Section 5 we outline our conclusions. We adopt $H_0 = 71$ km s^{-1} Mpc^{-1}, $\Omega_M = 0.27$ and $\Omega_\Lambda = 0.73$ throughout.

2. *NuSTAR* OBSERVATIONS AND MULTI-WAVELENGTH DATA

NuSTAR is the first high-energy (>10 keV) orbiting observatory with focusing optics and has a usable energy range of 3–79 keV (Harrison et al. 2013). *NuSTAR* consists of two co-aligned X-Ray Telescopes (XRTs; focal length of 10.14 m) which focus X-ray photons onto two independent shielded focal plane modules (FPMs), referred to here as FPMA and FPMB. Each FPM consists of four CdZnTe chips and has a ≈12′ × 12′ field of view at 10 keV; the pixel size is 2″.46. The focusing optics provide *NuSTAR* with a ≈1 order of magnitude improvement in angular resolution over previous observatories at >10 keV; the full width at half-maximum (FWHM) of the point-spread function (PSF) is ≈18″ and the half-power diameter is ≈58″. The absolute astrometric accuracy of *NuSTAR* is ±5″ (90%

confidence) for bright X-ray sources and the spectral resolution is ≈0.4 keV (FWHM) at 10 keV.

2.1. The NuSTAR Serendipitous Survey

The *NuSTAR* serendipitous survey is the largest-area component of the *NuSTAR* extragalactic survey program. The serendipitous survey is built up from *NuSTAR*-detected sources in the fields of *NuSTAR* targets, similar in principle to the serendipitous surveys undertaken in the fields of *Chandra* and *XMM-Newton* sources (e.g., Harrison et al. 2003; Kim et al. 2004; Watson et al. 2009). A major component of the *NuSTAR* serendipitous survey are ≈15–20 ks observations of ≈100 *Swift*-BAT identified AGNs, which provide both high-quality high-energy constraints of local AGNs and ≈2–3 deg^2 of areal coverage to search for serendipitous sources. However, the serendipitous survey is not restricted to these fields and the *NuSTAR* observations of targets not in the E-CDF-S, COSMOS, and Galactic-plane surveys are used to search for serendipitous *NuSTAR* sources; the exposures for these targets are also often substantially deeper than the *NuSTAR* observations of the *Swift*-BAT AGNs (up to on-axis exposures of 177.1 ks in the current paper). The expected areal coverage of the *NuSTAR* serendipitous survey in the first two years is ≈3–4 deg^2.

Using the *NuSTAR* data processing and source detection approach outlined below, at the time of writing we have serendipitously detected ≈50 sources in the fields of ≈70 *NuSTAR* targets. Here we present the properties of the first 10 spectroscopically identified sources; see Table 1. These 10 sources were selected from *NuSTAR* observations taken up until 2013 January 31. The selection of these sources for spectroscopic follow-up observations was based on their visibility to ground-based telescopes and they should therefore be representative of the overall high-energy source population.

2.1.1. Data Processing and Source Searching

The level 1 data products were processed with the NuSTAR Data Analysis Software (NuSTARDAS) package (v. 0.9.0). Event files (level 2 data products) were produced, calibrated, and cleaned using standard filtering criteria with the `nupipeline` task and the latest calibration files available in the *NuSTAR* CALDB. The *NuSTAR* observations of the Geminga field comprised 15 separate exposures, which we combined using XIMAGE v4.5.1;[24] the other *NuSTAR* observations reported here were individual exposures.

We produced 3–24 keV, 3–8 keV, and 8–24 keV images using DMCOPY from the Chandra Interactive Analysis Observations (CIAO) software (v4.4; Fruscione et al. 2006) for both *NuSTAR* FPMs.[25] We also produced exposure maps in each energy band for both FPMs, which take account of the fall in the effective area of the mirrors with off-axis angle and are normalized to the effective exposure of a source located at the aim point.

We searched for serendipitous sources in all of the six images (i.e., the three energy bands for each FPM) using WAVDETECT (Freeman et al. 2002) with an initial false-positive probability threshold of 10^{-6} and wavelet scales of 4, 5.66, 8, 11.31, and 16 pixels. To be considered a reliable *NuSTAR* source we require a detection to satisfy at least one of two criteria: (1) to be detected in at least one of the three images for both FPMA and FPMB;

---

[24] See http://heasarc.gsfc.nasa.gov/docs/xanadu/ximage/ximage.html for details of XIMAGE.

[25] See http://cxc.harvard.edu/ciao/index.html for details of CIAO.

Table 1
X-Ray Observations Used in the Paper

Target Field	HLX 1	NGC 1320	Geminga	SDSS J1157+6003	IC 751	NGC 4151	Cen X-4	WISE J1814+3412	3C 382	AE Aqr
Observatory	*NuSTAR*	*NuSTAR*	*NuSTAR*	*NuSTAR*	*NuSTAR*	*NuSTAR*	*NuSTAR*	*NuSTAR*	*NuSTAR*	*NuSTAR*
Observation	30001030002	60061036002	30001029(002–028)[b]	60001071002	60061217004	60001111005	30001004002	6000111402	60061286002	30001120004
Start date	2012 Nov 19	2012 Oct 25	2012 Sep 26	2012 Oct 28	2013 Feb 4	2012 Nov 14	2013 Jan 20	2012 Oct 30	2012 Sep 18	2012 Sep 5
Exposure[a]	177.1 ks	14.5 ks	142.6 ks	21.7 ks	56.1 ks	61.8 ks	116.4 ks	21.3 ks	16.6 ks	71.3 ks
Observatory	*Swift*-XRT	*Swift*-XRT	*Chandra*	*Chandra*	. . .	*Swift*-XRT	*XMM-Newton*	*XMM-Newton*	*Swift*-XRT	*XMM-Newton*
Observation	00031287003	00080314001	7592	5698	. . .	00080073001	0144900101	0693750101	00080217001	0111180201
Start date	2008 Nov 7	2012 Oct 26	2007 Aug 27	2005 Jun 3	. . .	2012 Nov 20	2003 Mar 1	2012 Oct 7	2012 Sep 18	2001 Nov 7
Exposure[a]	11.3 ks	6.8 ks	77.1 ks	7.0 ks	. . .	1.1 ks	55.3 ks	29.6 ks	6.6 ks	4.3 ks

Notes.
[a] The nominal on-axis exposure time (for *NuSTAR* the exposure is from FPMA), corrected for background flaring and bad events.
[b] The range of observation numbers that have been combined to produce the final image (only the 15 observations ending in even numbers are used).

or (2) to be detected in at least one of the three images in a single FPM but to have a lower-energy X-ray counterpart (e.g., detected by *Chandra*, *Swift*-XRT, or *XMM-Newton*). Following Section 3.4.1 of Alexander et al. (2003a), we also ran WAVDETECT at a false-positive probability threshold of 10^{-4} to search the six images (i.e., the three energy bands for each FPM) for lower significance counterparts of sources already detected at a false-positive probability threshold of 10^{-6} in any of the three energy bands.

See Tables 1 and 2 for the details of the X-ray data for the first 10 spectroscopically identified serendipitous *NuSTAR* sources. All of the *NuSTAR* sources are detected at >8 keV in at least one FPM.

2.1.2. Source Photometry

We measured the number of counts for each source at 3–24, 3–8, and 8–24 keV using either a $30''$, $45''$, or $60''$ radius circular aperture centered on the 3–24 keV WAVDETECT position for each FPM; the encircled-energy fractions of these apertures are ≈ 0.50, ≈ 0.66, and ≈ 0.77 of the full PSF, respectively, for a source at the aim point. The choice of aperture is dictated by the brightness of the source and how close it lies to another source; see Table 2 for the adopted aperture of each source. These measurements provide the gross source counts, which we correct for background counts to provide the net source counts. To obtain a good sampling of the background counts while minimizing the contribution to the background from the source counts, we measured the background in source-free regions using at least four circular apertures of $45''$ or $60''$ radius at least $90''$ from the source. The gross source counts are corrected for the background counts to give the net source counts, rescaling for the different sizes of the source and background regions. Errors on the net source counts are determined as the square root of the gross source counts. Upper limits are calculated when a source is not detected in one of the six images or if the net counts are less than the 1σ uncertainty; 3σ upper limits are calculated as three times the square root of the gross source counts. See Table 2 for the source photometry.

2.1.3. Source Fluxes

The source fluxes are calculated using the net count rates (i.e., the net counts divided by the source exposure time) and the measured X-ray spectral slope, following a procedure analogous to that used in the Chandra Deep Field surveys (e.g., Brandt et al. 2001; Alexander et al. 2003a). The X-ray spectral slope is determined from the band ratio, which we define here as the 8–24 keV/3–8 keV count-rate ratio. To convert the band ratio into an X-ray spectral slope we used XSPEC v12.7.1d (Arnaud 1996) and the response matrix file (RMF) and ancillary response file (ARF) of the detected *NuSTAR* sources; we produced the RMF and ARF following Section 2.1.5. We also used XSPEC and the RMF and ARF to determine the relationship between count rate, X-ray spectral slope, and source flux in each of the three energy bands: 3–24 keV, 3–8 keV, and 8–24 keV. We calculated the source fluxes in the three energy bands using the observed count rate and the derived X-ray spectral slope; for the faint *NuSTAR* sources with <100 net counts summed over the two FPMs, we set the X-ray spectral slope to $\Gamma = 1.8$, consistent with the average X-ray spectral slope of the overall sample (see Section 4.3). The source fluxes in each band were then corrected to the 100% encircled-energy fraction of the PSF and averaged over the two FPMs.

2.1.4. Source Positions

To provide the most accurate *NuSTAR* source positions and assist in source matching, we calculated a counts-weighted source position. This is determined from the 3–24 keV net counts and the 3–24 keV source position in each FPM. If a source is only detected in one FPM at 3–24 keV then the position of the source in that FPM is used.[26]

2.1.5. Extraction of the X-Ray Spectral Products

We extracted the *NuSTAR* data to be used in the X-ray spectral fitting analyses. The *NuSTAR* data were extracted using the *NuSTAR*-developed software `nuproducts`. `nuproducts` extracts source and background spectra and produces the RMF and ARF required to fit the X-ray data; the source and background spectra were extracted from each FPM using the same-sized apertures and regions as those adopted for the source photometry.

For the serendipitous source in the Geminga field (NuSTAR J063358+1742.4) we combined the source and background spectrum from each of the 15 observations (see Section 2.1.1) to produce a total source and background spectrum. We also produced an average ARF file for NuSTAR J063358+1742.4 by combining the individual ARF files, weighted by the exposure time for each ARF, and we used the RMF produced from the first observation when fitting the X-ray data.

2.2. Lower-energy X-Ray Data

To extend the X-ray spectral fitting constraints and assist in the identification of optical counterparts, we searched for <10 keV counterparts for each *NuSTAR*-detected source using *Chandra*, *Swift*-XRT, and *XMM-Newton* observations. Since the *NuSTAR* serendipitous program targets fields containing well-known Galactic and extragalactic targets, they all have lower-energy X-ray coverage. However, the only lower-energy X-ray data available in the IC 751 field is a short (≈ 2.3 ks) *Swift*-XRT observation in which the serendipitous *NuSTAR* source is detected with only 10 counts by XRT, which is insufficient to provide useful <10 keV constraints. For all of the other *NuSTAR* sources there are good-quality <10 keV data and, in some cases, there was more than one observation available. When selecting suitable lower-energy data we preferentially chose contemporaneous observations (i.e., observations taken within ≈ 1 week of the *NuSTAR* observations), which was the case for three sources in our sample (NuSTAR J032459-0256.1, NuSTAR J121027+3929.1, and NuSTAR J183443+3237.8). In the absence of contemporaneous observations we used existing lower-energy data where the 3–8 keV flux agreed to within a factor of two with the 3–8 keV flux measured from the *NuSTAR* data; see Section 2.3 for more details.

2.2.1. Chandra, Swift-XRT, and XMM-Newton Observations

The archival *Chandra* observations are analyzed using CIAO. The data were reprocessed using the `chandra_repro` pipeline to create the new level 2 event file, and the *Chandra* source spectra were extracted from a circular region with a radius of $\approx 5''$–$10''$. The background spectra were extracted from

---

[26] We derive the *NuSTAR* source name from the counts-weighted *NuSTAR* source position, adjusted to an appropriate level of precision (based on the *NuSTAR* positional accuracy), using the International Astronomical Union (IAU) approved naming convention for *NuSTAR* sources: NuSTAR JHHMMSS±DDMM.m, where m is the truncated fraction of an arcminute in declination for the arcseconds component.

5

Table 2
NuSTAR Source Properties

Target Field Source Name[a]	HLX 1 011042-4604.2	NGC 1320 032459-0256.1	Geminga 063358+1742.4	SDSS J1157+6003 115746+6004.9	IC 751 115912+4232.6	NGC 4151 121027+3929.1	Cen X4 145856-3135.5	WISE J1814+3412 181428+3410.8	3C 382 183443+3237.8	AE Aqr 204021-0056.1
R.A. (J2000)[b]	01:10:42.7	03:24:59.5	06:33:58.2	11:57:46.2	11:59:12.4	12:10:27.0	14:58:56.6	18:14:28.2	18:34:43.6	20:40:21.0
Decl. (J2000)[b]	−46:04:17	−02:56:09	+17:42:25	+60:04:55	+42:32:37	+39:29:07	−31:35:34	+34:10:51	+32:37:52	−00:56:06
Exposure (A)[c]	159.8	8.0	92.4	18.2	31.0	42.1	27.4	18.4	9.2	52.4
Exposure (B)[c]	159.4	5.9	93.0	18.5	31.2	39.9	46.0	20.0	9.6	51.7
3–24 keV (A)[d]	295 ± 35	129 ± 17	102 ± 24	(31 ± 12)	213 ± 20	621 ± 34	34 ± 22	<28	43 ± 12	148 ± 27
3–8 keV (A)[d]	172 ± 25	90 ± 13	51 ± 16	(24 ± 9)	132 ± 14	477 ± 28	<33	<19	(20 ± 8)	92 ± 19
8–24 keV (A)[d]	123 ± 25	38 ± 11	52 ± 18	<18	82 ± 14	145 ± 20	<36	(16 ± 9)	(24 ± 8)	57 ± 19
3–24 keV (B)[d]	265 ± 37	97 ± 14	(87 ± 31)	35 ± 12	262 ± 24	655 ± 33	28 ± 19	23 ± 12	52 ± 11	107 ± 24
3–8 keV (B)[d]	158 ± 26	62 ± 10	59 ± 22	19 ± 8	156 ± 17	494 ± 27	<25	(14 ± 8)	30 ± 8	77 ± 18
8–24 keV (B)[d]	109 ± 26	35 ± 10	<50	(16 ± 8)	108 ± 17	172 ± 19	29 ± 15	(9 ± 9)	(22 ± 7)	<37
Aperture[e]	45	60	45	45	45	30	45	45	45	45
Flux (3–24 keV)[f]	1.3	9.2	0.8	1.2[h]	5.6	12.1	0.6[h]	0.9[h]	3.5[h]	1.6
Flux (3–8 keV)[f]	0.4	3.9	0.3	0.5[h]	1.9	6.7	<0.2[h]	0.3[h]	1.1[h]	0.7
Flux (8–24 keV)[f]	0.8	5.8	0.6	0.7[h]	4.1	5.9	0.9[h]	0.7[h]	3.2[h]	1.0
X-ray offset[g]	4.3	7.6	0.9	4.6	. . .	4.9	6.5	9.9	8.6	4.5
Flux (3–8 keV; other data)[i]	0.8	2.7	0.2	0.8	. . .	7.5	0.4	0.4	1.5	0.7

Notes.

[a] Source name (NuSTAR J), based on the counts-weighted *NuSTAR* source position following the IAU source-name convention (see Footnote 26).

[b] Counts-weighted *NuSTAR* source position measured in the 3–24 keV energy band (see Section 2.1.4).

[c] Effective exposure at the source position in FPMA and FPMB in units of ks. The effective exposure is measured from the exposure maps (see Section 2.1.1).

[d] Net counts, 1σ uncertainties, and 3σ upper limits measured at the counts-weighted *NuSTAR* source position in the 3–24 keV, 3–8 keV, and 8–24 keV bands for FPMA and FPMB (see Section 2.1.2). The values in parentheses indicate a lower significance counterpart (see Section 2.1.1).

[e] Radius (in arcseconds) of the circular aperture used to measure the source photometry (see Section 2.1.2).

[f] Aperture-corrected flux in the 3–24 keV, 3–8 keV, and 8–24 keV energy bands in units of 10^{-13} erg s^{-1} cm^{-2} (see Section 2.1.3).

[g] Positional offset (in arcseconds) between the counts-weighted *NuSTAR* source position and the closest source detected in the lower-energy X-ray data (i.e., *Chandra*, *Swift*-XRT, *XMM-Newton*). See Table 1.

[h] Low-count source and $\Gamma = 1.8$ is used to convert the *NuSTAR* count rates into fluxes.

[i] Flux at 3–8 keV measured from the lower-energy X-ray data (either *Chandra*, *Swift*-XRT, or *XMM-Newton*; see Table 1) in units of 10^{-13} erg s^{-1} cm^{-2} (see Section 2.2).

several source-free regions of $\approx 40''$ radius, selected at different positions around the source to account for local background variations.

The *Swift*-XRT data are reduced using the HEAsoft (v.6.12) pipeline xrtpipeline, which cleans the event files using appropriate calibration files and extracts the spectra and ancillary files for a given source position;[27] the source extraction regions had radii of $\approx 20''$. Since the background in the *Swift*-XRT observations is very low, no background spectra were extracted.

For the *XMM-Newton* EPIC data we used the Pipeline Processing System products, which are a collection of standard processed high-quality products generated by the Survey Science Center. For our analysis we used the Science Analysis Software (SAS v.12.0.1), released in 2012 June.[28] After filtering the event files for high background intervals, we extracted the source spectra from a circular region with a radius of $\approx 20''$. The corresponding background spectra have been extracted using circular source-free regions in the vicinity of the corresponding source ($\approx 30''$–$60''$ radius regions). Using the SAS tasks rmfgen and arfgen we also produced the response matrices for each source in each of the three EPIC cameras separately (pn, MOS1, and MOS2).

2.3. Counterpart Matching

To provide reliable source identification we matched the *NuSTAR* sources to the <10 keV and multi-wavelength data; see Sections 2.2 and 2.4, and Table 3 for the description of the data. We searched for multi-wavelength counterparts within $10''$ of the *NuSTAR* source positions using on-line source catalogs and multi-wavelength images; the latter approach is required for faint counterparts or for recent data not yet reported in on-line source catalogs. The $10''$ search radius is motivated by the absolute astrometric accuracy of *NuSTAR* ($\pm 5''$, 90% confidence, for bright X-ray sources; Harrison et al. 2013) and the low count rates for the majority of our sources.

A lower-energy X-ray counterpart is found within $10''$ for each of the *NuSTAR* sources; see Table 2. To provide further confidence that the X-ray source is the correct lower-energy counterpart to the *NuSTAR* source, we compared the 3–8 keV fluxes of the lower-energy source and the *NuSTAR* source. We selected and extracted the lower-energy X-ray data following Section 2.2 and we calculated the 3–8 keV fluxes using a power-law model in XSPEC (the model component is POW in XSPEC); see Table 1 for details of the low-energy X-ray data selected for each source. The average source flux was calculated for the *XMM-Newton* data when multiple detectors were used (i.e., pn, MOS 1 and MOS 2). In Figure 1 we compare the 3–8 keV fluxes from the lower-energy X-ray data to the 3–8 keV flux from the *NuSTAR* data. In all cases the fluxes agree within a factor of two, demonstrating that we have selected the correct lower-energy X-ray counterpart.

An optical counterpart is also found within $10''$ of each *NuSTAR* source; see Table 3. Given the larger intrinsic uncertainty in the *NuSTAR* source position when compared to the lower-energy X-ray source position, we also measured the distance between the lower-energy X-ray source position and the optical position. An optical counterpart is found within $3''$ (and the majority lie within $1''$) of the lower-energy X-ray source position for all of the sources. See Figure 2 for example multi-wavelength cut-out images of NuSTAR J183443+3237.8 in the 3C 382 field.
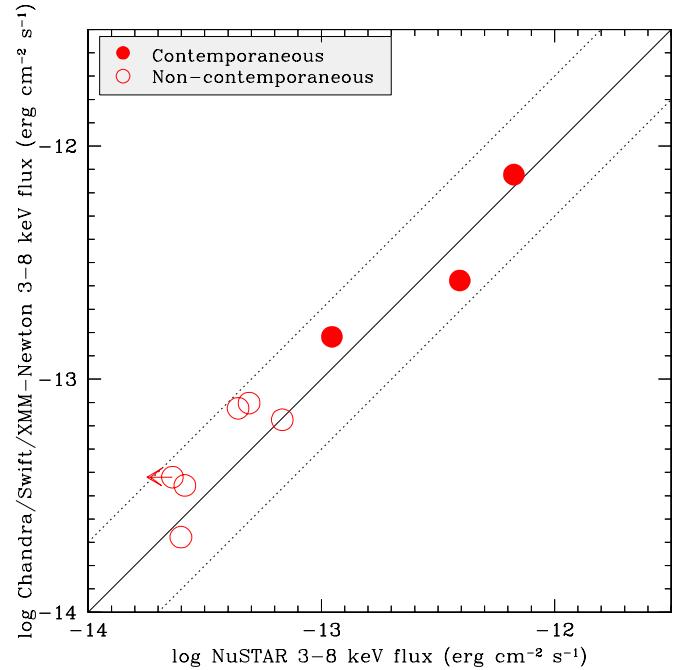

Figure 1. Comparison of the measured fluxes in the 3–8 keV band between *NuSTAR* and lower-energy X-ray observations (*Chandra*, *Swift*-XRT, or *XMM-Newton*); see Table 1 for details of the data used for each source. The filled circles indicate sources where the lower-energy observations were obtained within 1 week of the date of the *NuSTAR* observations and the unfilled circles indicate sources where the lower-energy observations were obtained more than 1 week after the *NuSTAR* observations. The solid line indicates agreement between the fluxes while the dotted lines indicate a factor of two disagreement between the fluxes.

(A color version of this figure is available in the online journal.)

2.4. Ultraviolet–Radio Data

To further characterize the properties of the *NuSTAR* sources we used ultraviolet (UV) to mid-infrared (MIR) data. Table 3 presents the broad-band UV–MIR photometric properties of the *NuSTAR* sources, primarily obtained from existing, publicly available all-sky or large-area surveys, including the *Galaxy Evolution Explorer* (*GALEX*; Martin et al. 2005), the Digitized Sky Survey (DSS; Minkowski & Abell 1963; Hambly et al. 2001), the Sloan Digital Sky Survey (SDSS; York et al. 2000), the Two Micron All Sky Survey (2MASS; Skrutskie et al. 2006), and the *Wide-field Infrared Survey Explorer* (*WISE*; Wright et al. 2010). The source photometry is provided in its native format for all of the sources. The DSS data, provided for sources outside of the SDSS, were obtained from the SuperCOSMOS scans of the photographic Schmidt plates (Hambly et al. 2001). As recommended by the SuperCOSMOS Sky Survey, all photometric uncertainties are set to 0.30 mag for those measurements. Where publicly available, we also provide *Spitzer* photometry from the Infrared Array Camera (IRAC; Fazio et al. 2004), obtained from the post-basic calibrated data (PBCD) products. To avoid the effects of source confusion, photometry was measured in $2''.4$ radius apertures on the $0''.6$ pixel^{-1} resampled PBCD mosaics, and then corrected to total flux density using aperture corrections from the IRAC Instrument Handbook (v.2.0.2).[29] Several sources were observed during the post-cryogenic *Warm Spitzer* phase, and thus only the two shorter wavelength bandpasses from *Spitzer*-IRAC are available.

---

[27] See http://heasarc.gsfc.nasa.gov/docs/software/lheasoft/ for details of HEAsoft.
[28] See http://xmm.esa.int/sas/ for details of the SAS software.

[29] See http://irsa.ipac.caltech.edu/data/SPITZER/docs/irac/ for details of *Spitzer*-IRAC.

Table 3
Ultraviolet-to-Mid-infrared Source Properties

Target Field Source Name[a]	HLX 1 011042-4604.2	NGC 1320 032459-0256.1	Geminga 063358+1742.4	SDSS J1157+6003 115746+6004.9	IC 751 115912+4232.6	NGC 4151 121027+3929.1	Cen X4 145856-3135.5	WISE J1814+3412 181428+3410.8	3C 382 183443+3237.8	AE Aqr 204021-0056.1
R.A. (J2000)[b]	01:10:43.08	03:24:59.95	06:33:58.22	11:57:46.75	11:59:12.20	12:10:26.61	14:58:57.05	18:14:28.82	18:34:43.23	20:40:20.71
Decl. (J2000)[b]	−46:04:20.0	−02:56:12.1	+17:42:24.2	+60:04:52.9	+42:32:35.4	+39:29:08.4	−31:35:37.8	+34:10:51.2	+32:37:54.4	−00:56:06.0
Optical offset[c]	4.7 (0.8)	7.7 (0.5)	1.4 (1.1)	4.5 (0.1)	2.5	4.5 (0.5)	7.4 (1.3)	8.1 (1.9)	6.0 (2.9)	4.3 (0.2)
FUV[d]	...	19.49 ± 0.12	...	...	...	21.81 ± 0.45	...	...	23.33 ± 0.29	...
NUV[d]	21.92 ± 0.45	19.02 ± 0.06	...	...	22.31 ± 0.46	21.01 ± 0.22	...	21.07 ± 0.23	21.90 ± 0.05	23.70 ± 0.25
u[d]	...	...	...	24.5 ± 1.1	21.61 ± 0.40	20.02 ± 0.04	...	...	...	23.84 ± 0.82
g/B[‡d]	...	...	...	22.29 ± 0.13	19.34 ± 0.02	19.72 ± 0.01	...	21.19 ± 0.08	21.63 ± 0.45[‡]	22.43 ± 0.14
r/R[‡d]	...	16.3[‡]	...	21.56 ± 0.09	18.14 ± 0.01	19.42 ± 0.01	19.9[‡]	20.62 ± 0.07	19.54 ± 0.18[‡]	21.56 ± 0.10
i/I[‡d]	...	...	...	21.53 ± 0.13	17.59 ± 0.01	19.06 ± 0.01	...	...	18.67 ± 0.20[‡]	20.37 ± 0.06
z[d]	...	...	...	21.52 ± 0.47	17.24 ± 0.03	18.79 ± 0.04	...	...	...	20.35 ± 0.22
J[d]	...	14.89 ± 0.06	>19.8	...	16.59 ± 0.14	...	...	...	...	...
H[d]	...	14.37 ± 0.09	...	...	16.18 ± 0.17	...	...	...	...	...
K_s[d]	...	14.06 ± 0.09	...	...	15.09 ± 0.11	...	...	...	...	...
WISE W1 (3.4 μm)[d]	15.98 ± 0.07	13.20 ± 0.03	...	16.77 ± 0.10	14.10 ± 0.03	14.86 ± 0.04	16.91 ± 0.16	...	15.32 ± 0.04	16.05 ± 0.08
WISE W2 (4.6 μm)[d]	15.44 ± 0.13	13.00 ± 0.03	...	15.63 ± 0.13	12.97 ± 0.03	14.59 ± 0.64	15.19 ± 0.12	...	14.31 ± 0.05	15.05 ± 0.10
WISE W3 (12 μm)[d]	12.48 ± 0.39	9.87 ± 0.05	...	12.89 ± 0.47	9.70 ± 0.04	...	...	11.54 ± 0.19	11.38 ± 0.11	11.89 ± 0.26
WISE W4 (22 μm)[d]	...	7.70 ± 0.14	...	...	6.87 ± 0.09	...	...	...	8.62 ± 0.26	...
Spitzer (3.6 μm)[d]	...	...	48.78 ± 0.33	...	639.2 ± 1.1	236.79 ± 0.47	...	85.74 ± 0.80	...	...
Spitzer (4.5 μm)[d]	...	...	54.13 ± 0.22	...	1022.07 ± 0.76	204.72 ± 0.48	...	151.22 ± 0.74	...	...
Spitzer (5.8 μm)[d]	...	...	62.4 ± 1.7	...	...	...	...	...	...	...
Spitzer (8.0 μm)[d]	...	...	114.6 ± 2.0	...	...	...	...	...	...	...
Redshift[e]	1.073	0.020	0.891	2.923	0.177	0.615	1.045	0.763	0.510	0.601
Telescope[f]	Gemini-S	Keck	Keck	P200	P200	...	...	Keck	P200	Keck
Camera[f]	GMOS-S	LRIS	LRIS	DBSP	DBSP	...	...	LRIS	DBSP	DEIMOS
UT date[f]	2012 Dec 12	2012 Nov 9	2013 Jan 10	2012 Nov 20	2012 Nov 20	...	...	2012 Nov 9	2012 Oct 10	2012 Oct 13
Type[f]	BLAGN	NLAGN	NLAGN	BLAGN	NLAGN	BL Lac object	BLAGN	BLAGN	BLAGN	NLAGN
$\hat{a}$[g]	0.43 ± 0.14	0.25 ± 0.03	0.84 ± 0.04	0.77 ± 0.09	0.70 ± 0.01	0.50 ± 0.03	1.00 ± 0.04	0.77 ± 0.05	0.67 ± 0.04	0.76 ± 0.04
$E(B-V)$[g]	2.0 ± 4.6	0.1 ± 0.1	4.2 ± 2.9	0.1 ± 0.4	5.9 ± 0.6	0.04 ± 0.01	0.0 ± 0.1	2.5 ± 1.0	0.6 ± 0.5	3.2 ± 1.3
$L_{6\,\mu m}$[g]	3.6 ± 2.5	0.004 ± 0.001	2.6 ± 1.4	29.9 ± 14.3	0.9 ± 0.1	2.1 ± 0.2	6.8 ± 0.8	4.7 ± 1.1	2.0 ± 0.2	2.2 ± 0.5
M_*[g]	334 ± 51	2.0 ± 0.1	114 ± 25	2000 ± 340	88 ± 3	236 ± 18	<41	68 ± 17	117 ± 20	121 ± 13

Notes.

[a] Source name (NuSTAR J); see Table 2.

[b] Counterpart source position.

[c] Positional offset (in arcseconds) between the counts-weighted *NuSTAR* position and the counterpart source position (the value in parentheses gives the positional offset between the lower-energy X-ray source and the counterpart source position).

[d] Source photometry given in its native format (e.g., AB mag for *GALEX*, AB sinh mag for SDSS, μJy for *Spitzer*, and Vega mag for all others unless otherwise noted). Optical photometry with double-dagger symbol (‡) indicates when the given measurements are not from the SDSS; the photometry for these sources is obtained from the DSS, via SuperCOSMOS unless otherwise noted in the text (see Section 2.4). For the Geminga serendipitous source, we obtained *J*-band imaging from the KPNO 2.1 m telescope (see Section 2.4).

[e] Optical spectroscopic redshift, as described in Section 2.5, except for NuSTAR J121027+3929.1 and NuSTAR J145856-3135.5, which are taken from Morris et al. (1991) and Caccianiga et al. (2008), respectively.

[f] Observational details of the optical spectroscopy and the optical spectroscopic classification, as given in Sections 2.5 and 4.1, and the Appendix (see Morris et al. 1991 and Caccianiga et al. 2008 for details of NuSTAR J121027+3929.1 and NuSTAR J145856-3135.5).

[g] Best-fitting parameters and 1σ uncertainties from the UV–mid-infrared SED fitting (see Section 3.2): $\hat{a}$ is the fractional contribution to the UV–MIR emission from the AGN component, $E(B-V)$ is the dust reddening (units of mag), $L_{6\,\mu m}$ is the infrared luminosity of the AGN at rest-frame 6 μm (νL_ν) in units of 10^{44} erg s^{-1}, and M_* gives the stellar mass (units of $10^9\,M_\odot$).
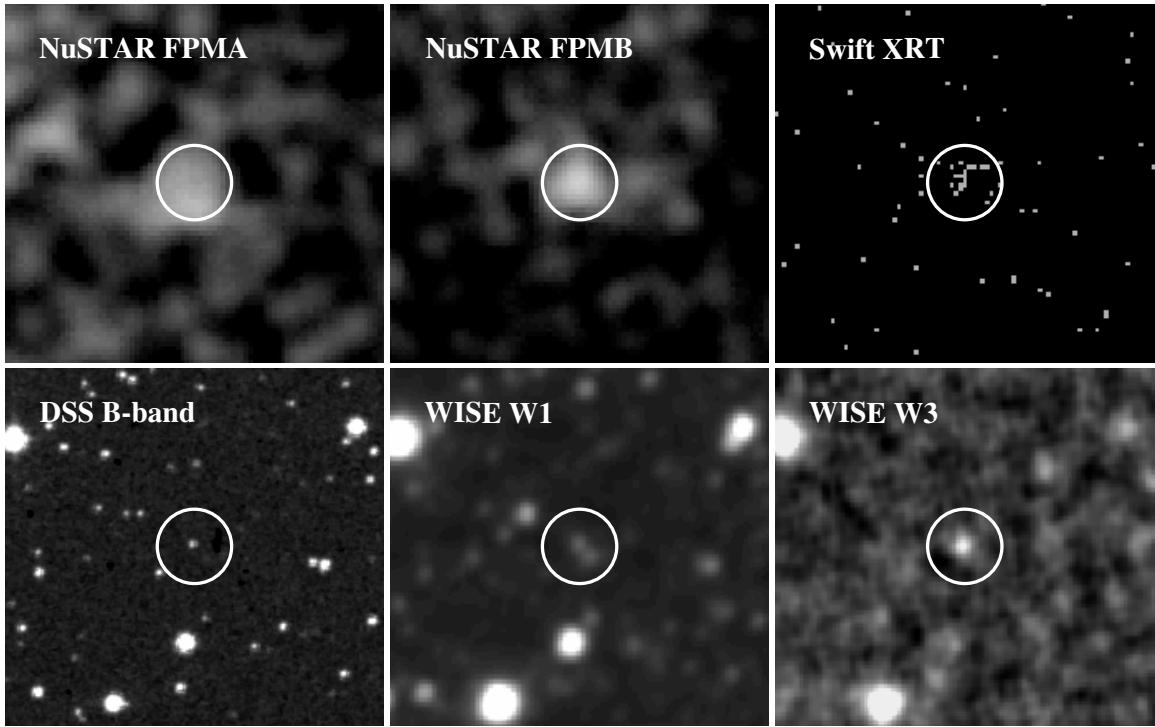
Figure 2. Example multi-wavelength cut-out images to demonstrate some of the quality of the multi-wavelength data. The object shown here is NuSTAR J183443+3237.8 in the 3C 382 field, a faint *NuSTAR* source. The images are (from top left to bottom right): *NuSTAR* 3–24 keV FPMA, *NuSTAR* 3–24 keV FPMB, *Swift*-XRT 0.5–10 keV, DSS *B*-band, *WISE* band 1 (W1; 3.4 μm), and *WISE* band 3 (W3; 12 μm); the *NuSTAR* images have been smoothed with a 6 pixel (14″8) Gaussian. The circle has a radius of 20″ and is centered on the *NuSTAR* source position.

In several cases we used photometry from different sources, which we list below. For NuSTAR J063358+1742.4 we report a *J*-band non-detection, which is measured from 1.56 ks of dithered observations obtained with the Florida Infrared Imaging Multi-object Spectrograph on the Kitt Peak 2.1 m telescope. The data were obtained on UT 2012 October 17 in photometric but 1″6 seeing conditions, and the 3σ upper limit was calculated in a 2″ radius aperture; see Table 3 for more details. For NuSTAR J145856-3135.5 we report the *R*-band magnitude from Caccianiga et al. (2008). For NuSTAR J181428+3410.8 the optical photometry comes from imaging reported in Eisenhardt et al. (2012), calibrated to the SDSS. The *WISE* 12 μm photometry for NuSTAR J181428+3410.8 was measured directly from the images as this source does not appear in the WISE All-Sky Catalog; we do not provide the shorter wavelength *WISE* photometry for this source as it is superseded by *Warm Spitzer* observations. For NuSTAR J183443+3237.8 we obtained *B*-, *R*-, and *I*-band observations using the Palomar 60 inch telescope (P60) on UT 2013 March 4 in ≈2″ seeing; the exposure time was 300 s in each band, repeated three times with a 60″ dither. NuSTAR J183443+3237.8 was well detected in all three bands and the reported photometry in Table 3 was measured in 4″ diameter apertures, which has been corrected for PSF losses.

We also searched for radio counterparts in the NVSS and FIRST VLA surveys (Becker et al. 1995; Condon et al. 1998), using a search radius of 30″ and 15″, respectively. NuSTAR J121027+3929.1 was detected in both surveys and has a flux of $f_{1.4\,\text{GHz}} = 18.7 \pm 0.7$ mJy (in the NVSS survey), which corresponds to a rest-frame luminosity density of $L_{1.4\,\text{GHz}} = 2.2 \times 10^{24}$ W Hz^{-1} (calculated following Equation (2) of Alexander et al. 2003b and assuming a radio spectral slope of $\alpha = 0.8$). With the exception of NuSTAR J011042-4604.2,

all of the other sources had at least NVSS coverage but none were detected. The rest-frame luminosity density upper limits ranged from $L_{1.4\,\text{GHz}} < 1.8 \times 10^{20}$ W Hz^{-1} (for NuSTAR J032459-0256.1) to $L_{1.4\,\text{GHz}} < 4.3 \times 10^{24}$ W Hz^{-1} (for NuSTAR J115746+6004.9), with the majority of the sources having upper limits of $L_{1.4\,\text{GHz}} < 10^{23}$–$10^{24}$ W Hz^{-1}.

2.5. Optical Spectroscopy

Two of the ten serendipitous sources have existing optical spectroscopy: NuSTAR J121027+3929.1 has been previously identified as a BL Lac object at $z = 0.615$ (MS 1207.9+3945; e.g., Stocke et al. 1985; Gioia et al. 1990; Morris et al. 1991) while NuSTAR J145856-3135.5 has been previously identified as a broad-line AGN (BLAGN) at $z = 1.045$ (2XMM J145857.0-313536; Caccianiga et al. 2008). For the other eight serendipitous *NuSTAR* sources we obtained optical spectroscopy at the Palomar, Keck, and Gemini-South telescopes. Table 3 presents basic information about the observations, including the instrument and UT date of the observations and in the Appendix we provide specific details for each observation. We processed all of the optical spectroscopic data using standard techniques, and flux calibrated the spectra using standard stars observed on the same nights.

The optical spectra for the eight newly identified *NuSTAR* sources are shown in Figure 3. Clear multiple broad and/or narrow emission lines are detected in six sources, showing that the redshift identifications are reliable. However, the optical counterparts for NuSTAR J115746+6004.9 and NuSTAR J063358+1742.4 are comparatively faint and the optical spectra are therefore of lower quality when compared to the optical spectra of the other serendipitous sources. NuSTAR J115746+6004.9 has narrow, spatially extended Lyα emission as well as
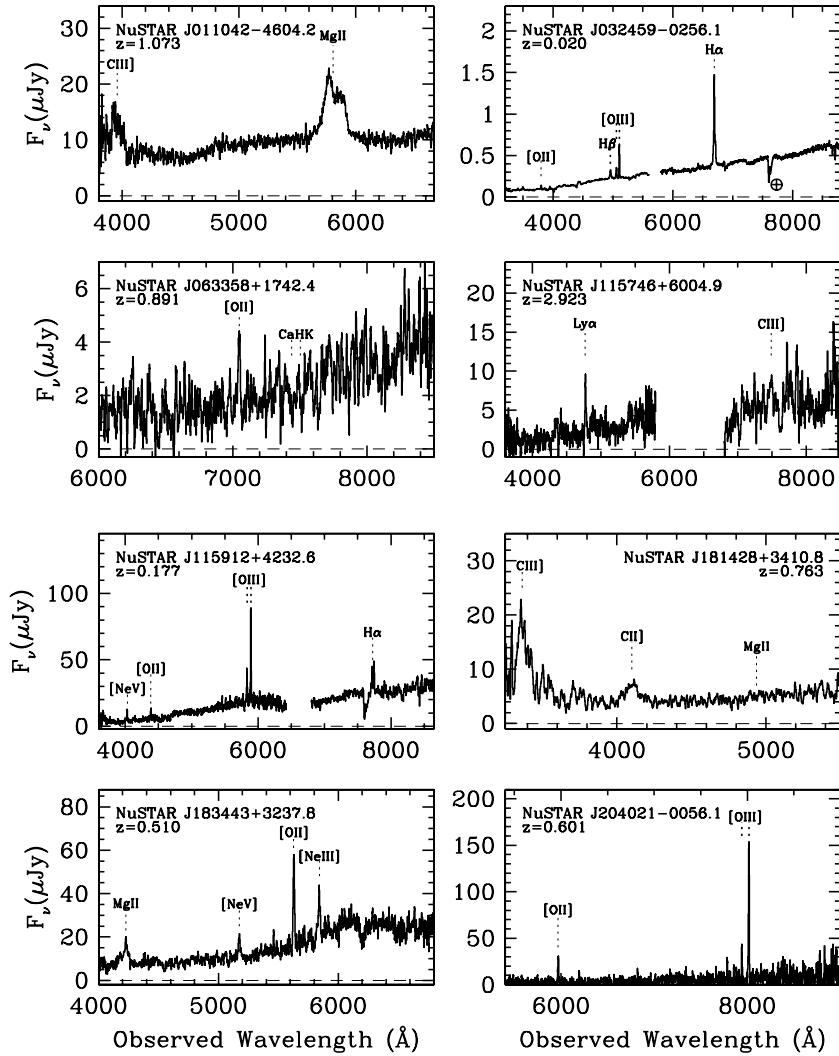
Figure 3. Optical spectra for the eight newly identified serendipitous *NuSTAR* sources; the optical spectra of the other two sources (NuSTAR J121027+3929.1 and NuSTAR J145856-3135.5) have been previously presented in Morris et al. (1991) and Caccianiga et al. (2008). The prominent emission and absorption lines are indicated; see Section 2.5.

somewhat broadened C III] emission indicating $z = 2.923$; spatially extended Lyα emission is often found to be associated with powerful AGNs (e.g., Reuland et al. 2003; Geach et al. 2009; Yang et al. 2009). The redshift of NuSTAR J063358+1742.4 is less certain due to the identification of a single narrow emission line, which is more likely to be [O II] at $z = 0.891$ than Lyα due to the rising optical continuum and lack of a strong Lyα forest decrement (as would be expected had the source been at $z \sim 4.8$); the identification of two absorption features at the wavelengths expected for Ca H+K provides additional confidence for $z = 0.891$. We consider all of the redshifts to be reliable.

The two *NuSTAR* sources with existing optical spectroscopy (NuSTAR J121027+3929.1; NuSTAR J145856-3135.5) have optical magnitudes consistent with the eight newly identified *NuSTAR* sources and meet our basic requirement for inclusion in this paper (i.e., sources identified in *NuSTAR* observations taken up until 2013 January 31); we note that several of the other ≈40 serendipitously detected *NuSTAR* sources also have existing optical spectroscopy but have been identified in more recent *NuSTAR* observations and so are not included in this paper. We therefore believe that the inclusion of these two *NuSTAR* sources does not bias our overall *NuSTAR* sample.

3. DATA ANALYSIS

3.1. X-Ray Spectral Fitting

To interpret the X-ray data and provide insight into the intrinsic AGN properties of the serendipitous *NuSTAR* sources (e.g., Γ and N_H) we fitted the X-ray data using physically motivated AGN models. We extracted the *NuSTAR* data following Section 2.1.5 and the lower-energy X-ray data following Section 2.2.1.

For the three sources with >200 counts in each *NuSTAR* FPM at 3–24 keV (NuSTAR J011042-4604.2, NuSTAR J115912+4232.6, and NuSTAR J121027+3929.1; see Table 2), we grouped the *NuSTAR* data into bins of at least 40 counts bin^{-1} and used χ^2 statistics to find the best-fitting model parameter solutions. However, the *NuSTAR* photon statistics were too poor to allow for χ^2 statistics for the other seven sources, and for the X-ray spectral analyses of these sources we fitted the unbinned X-ray data using the *C*-statistic (Cash 1979). The *C*-statistic is calculated on unbinned data and is therefore ideally suited to low-count sources (e.g., Nousek & Shue 1989). However, since the data need to be fitted without the background subtracted, it is essential to accurately characterize the background and use that as a fixed model component in the X-ray spectral fitting of the
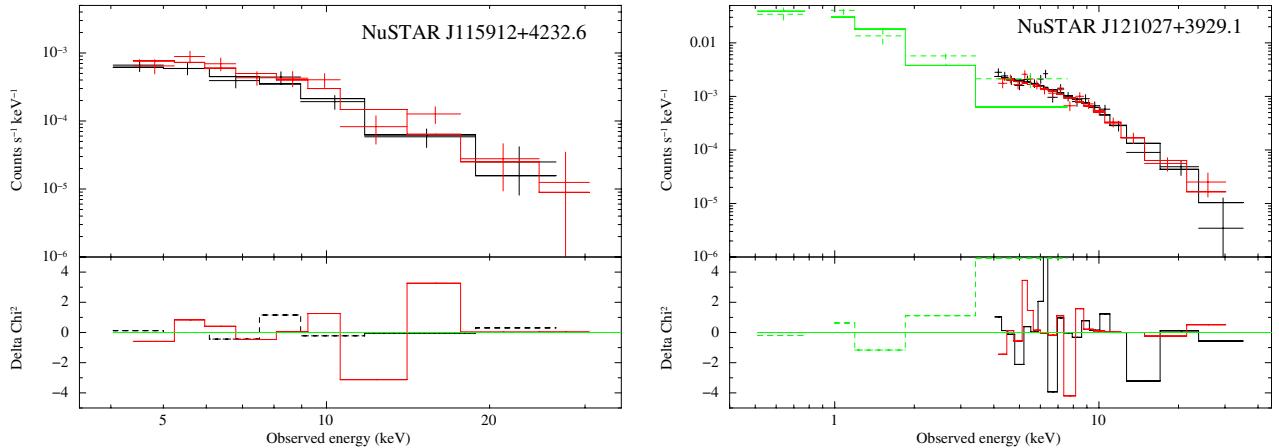
Figure 4. Example X-ray spectra and best-fitting power-law model solutions for NuSTAR J115912+4232.6 (left) and NuSTAR J121027+3929.1 (right). The *NuSTAR* data are plotted for NuSTAR J115912+4232.6 over 4–32 keV and the *NuSTAR* and *Swift*-XRT data are plotted for NuSTAR J121027+3929.1 over 0.5–50 keV. The black and red crosses are from *NuSTAR* FPMA and FPMB, respectively, and the green crosses are from *Swift*-XRT. The X-ray data have been grouped and fitted using a power-law model and χ^2 statistics; see Section 3.1. The best-fitting models are plotted as solid lines and the bottom panels show the deviations of the data from the best-fitting model ($\Delta \chi^2$).

(A color version of this figure is available in the online journal.)

source spectrum. We characterized the background by fitting the background regions using a double power-law model (the model components are POW*POW in XSPEC). The photon statistics were also often poor for the lower-energy X-ray data (<200 counts) and we therefore typically fitted the unbinned <10 keV data using the *C*-statistic with the measured background as a fixed component. In Figure 4 we show example *NuSTAR* spectra for two of the brightest *NuSTAR* sources: NuSTAR J115912+4232.6 and NuSTAR J121027+3929.1; for NuSTAR J121027+3929.1 we also show the *Swift*-XRT data. All fit parameter uncertainties are quoted at the 90% confidence level (Avni 1976).

We initially fitted only the *NuSTAR* data using a simple power-law model (the POW model in XSPEC) to provide constraints on the overall X-ray spectral slope (Γ) over 4–32 keV. We also restricted the *NuSTAR* data to cover the rest-frame 10–40 keV energy range for each source and fitted a power-law model to measure both the rest-frame 10–40 keV spectral slope ($\Gamma_{10-40\,\mathrm{keV}}$) and luminosity ($L_{10-40\,\mathrm{keV}}$); given the redshift of NuSTAR J115746+6004.9 ($z = 2.923$) we fitted to the rest-frame 15–60 keV data. See Table 4.

To provide direct measurements on the presence of absorption we jointly fitted an absorbed power-law model (the model components are ZWABS*POW in XSPEC) to both the *NuSTAR* and lower-energy X-ray data for each source.[30] For five of the sources we fitted the 0.5–32 keV data (for NuSTAR J121027+3929.1 we fitted the 0.5–50 keV data, given the good photon statistics of this source), jointly fitting the X-ray spectral slope and absorbing column density for both of the *NuSTAR* FPMs and the lower-energy X-ray data. However, for NuSTAR J115912+4232.6 no good-quality low-energy X-ray data exist and we therefore only fitted the *NuSTAR* data, while for the remaining three sources (NuSTAR J115746+6004.9, NuSTAR J145856-3135.5, and NuSTAR J181428+3410.8) the photon statistics of the *NuSTAR* data were too poor to provide reliable constraints on both Γ and N_{H}, and we therefore fitted the absorbed power-law model to just the lower-energy X-ray data. The best-fitting model parameters are given in Table 4.

3.2. Ultraviolet-Mid-infrared Spectral Energy Distribution Fitting

To constrain the relative contributions from AGN activity and the host galaxy to the UV–MIR data we fitted the broadband UV–MIR spectral energy distributions (SEDs) using the 0.03–30 μm empirical low-resolution templates for AGNs and galaxies of Assef et al. (2010). Each SED is modeled as the best-fit non-negative combination of three galaxy templates and an AGN template. The reddening of the AGN template, parameterized by $E(B-V)$, is a free parameter in the fit. The errors on the parameters were calculated using a Monte Carlo method, where the photometry is resampled 1000 times according to the photometric uncertainties and the SED fits and parameters are recalculated; the errors refer to the standard deviation for all of the realizations. Since the templates have been empirically defined using AGNs with similar X-ray luminosities and redshifts as the *NuSTAR* sources, we do not expect there to be significant systematic uncertainties in the best-fitting model solutions; the efficacy of the SED-fitting approach will be further explored in S. M. Chung et al. (in preparation). We refer the reader to Assef et al. (2008, 2010, 2013) for further details.

In Figure 5 we present the UV–MIR SEDs and best-fitting solutions and in Table 3 we provide the following best-fitting parameters: $\hat{a}$ (the fractional contribution to the overall emission from the AGN component over 0.1–30 μm; Assef et al. 2013), $E(B-V)$ (the dust reddening of the AGN component), $L_{6\,\mu\mathrm{m}}$ (the luminosity of the AGN component at rest-frame 6 μm), and M_* (the stellar mass of the host galaxy). The stellar mass is calculated from the absolute magnitude of the stellar component using the color–magnitude calibration of Bell et al. (2003). Three of the *NuSTAR* sources have photometric measurements in $\leqslant 5$ bands (NuSTAR J11042+4604.2, NuSTAR J063358+1742.4, and NuSTAR J145856-3135.5) and the derived properties for these sources are therefore poorly constrained.

4. RESULTS

In analyzing the *NuSTAR* sources we predominantly focus on characterizing their X-ray and UV–MIR properties and comparing these properties to those of sources detected in previous-generation $\gtrsim 10$ keV surveys (e.g.,

---

[30] We note that AGNs often require more complex models to characterize their X-ray emission than that of a simple absorbed power law (e.g., Winter et al. 2009; Vasudevan et al. 2013). However, the data quality of our sources is not sufficient to reliably constrain such models on a source by source basis (see Section 4.3 for more detailed average constraints).

Table 4
Best-fitting Model Parameters

Target Field Source Name[a]	HLX 1 011042-4604.2	NGC 1320 032459-0256.1	Geminga 063358+1742.4	SDSS J1157+6003 115746+6004.9	IC 751 115912+4232.6	NGC 4151 121027+3929.1	Cen X4 145856-3135.5	WISE J1814+3412 181428+3410.8	3C 382 183443+3237.8	AE Aqr 204021-0056.1
Data fitted[b]	*NuSTAR*	*NuSTAR*	*NuSTAR*	*NuSTAR*	*NuSTAR*	*NuSTAR*	*NuSTAR*	*NuSTAR*	*NuSTAR*	*NuSTAR*
Energy range[c]	4–32	4–32	4–32	4–32	4–32	4–50	4–32	4–32	4–32	4–32
Γ[d]	$1.9^{+0.4}_{-0.3}$	$2.2^{+0.5}_{-0.5}$	$1.6^{+0.6}_{-0.5}$	$2.2^{+0.8}_{-0.7}$	$1.9^{+0.3}_{-0.3}$	$2.4^{+0.2}_{-0.1}$	$0.5^{+1.2}_{-1.3}$	$1.9^{+7.4}_{-2.5}$	$1.5^{+0.7}_{-0.6}$	$1.6^{+0.5}_{-0.5}$
$\Gamma_{10\text{–}40\,\mathrm{keV}}$[e]	$1.9^{+0.5}_{-0.5}$	$1.2^{+1.9}_{-1.2}$	$2.0^{+0.7}_{-0.6}$	$1.9^{+0.8}_{-0.8}$	$1.8^{+1.3}_{-0.9}$	$2.4^{+0.3}_{-0.3}$	$0.4^{+1.4}_{-1.4}$	$0.4^{+2.2}_{-0.4}$	$1.7^{+1.1}_{-0.9}$	$2.3^{+0.9}_{-0.8}$
$L_{10\text{–}40\,\mathrm{keV}}$[e]	5.0	0.0049	2.7	82	0.37	13	4.5	1.7	2.9	1.7
Data fitted[b]	*NuSTAR* +*Swift*-XRT	*NuSTAR* +*Swift*-XRT	*NuSTAR* +*Chandra*	*Chandra*	*NuSTAR*	*NuSTAR* +*Swift*-XRT	*XMM-Newton*	*XMM-Newton*	*NuSTAR* +*Swift*-XRT	*NuSTAR* +*XMM-Newton*
Energy range[c]	0.5–32	0.5–32	0.5–32	0.5–8	4–32	0.5–50	0.5–12	0.5–12	0.5–32	0.5–32
Γ[f]	$2.0^{+0.3}_{-0.3}$	$2.0^{+0.4}_{-0.3}$	$1.6^{+0.5}_{-0.5}$	$1.9^{+0.8}_{-0.6}$	$2.2^{+1.2}_{-0.6}$	$2.4^{+0.2}_{-0.1}$	$1.9^{+0.3}_{-0.3}$	$1.9^{+0.5}_{-0.4}$	$1.4^{+0.5}_{-0.5}$	$1.8^{+0.5}_{-0.5}$
N_{H}[f]	$1.4^{+1.4}_{-1.1}$	<0.2	$10.9^{+5.6}_{-4.2}$	<11.9	<65.4	<0.6	<0.9	$1.9^{+1.1}_{-0.8}$	<1.5	$10.2^{+12.4}_{-5.7}$

Notes.

[a] Source name (NuSTAR J); see Table 2.

[b] Origin of the X-ray data used in the spectral fitting.

[c] Observed-frame energy range (in keV) over which the X-ray data are fitted.

[d] Best-fitting spectral slope (Γ) and uncertainty (90% confidence) over the full spectral range for a power-law model.

[e] Best-fitting spectral slope (Γ), uncertainty (90% confidence), and luminosity (units of 10^{44} erg s^{-1}) from fitting the rest-frame 10–40 keV data with a power-law model (see Section 3.1 for more details).

[f] Best-fitting spectral slope (Γ), absorbing column density, uncertainty (90% confidence), and upper limits (N_{H}; units of 10^{22} cm^{-2}; see Section 3.1 for more details).
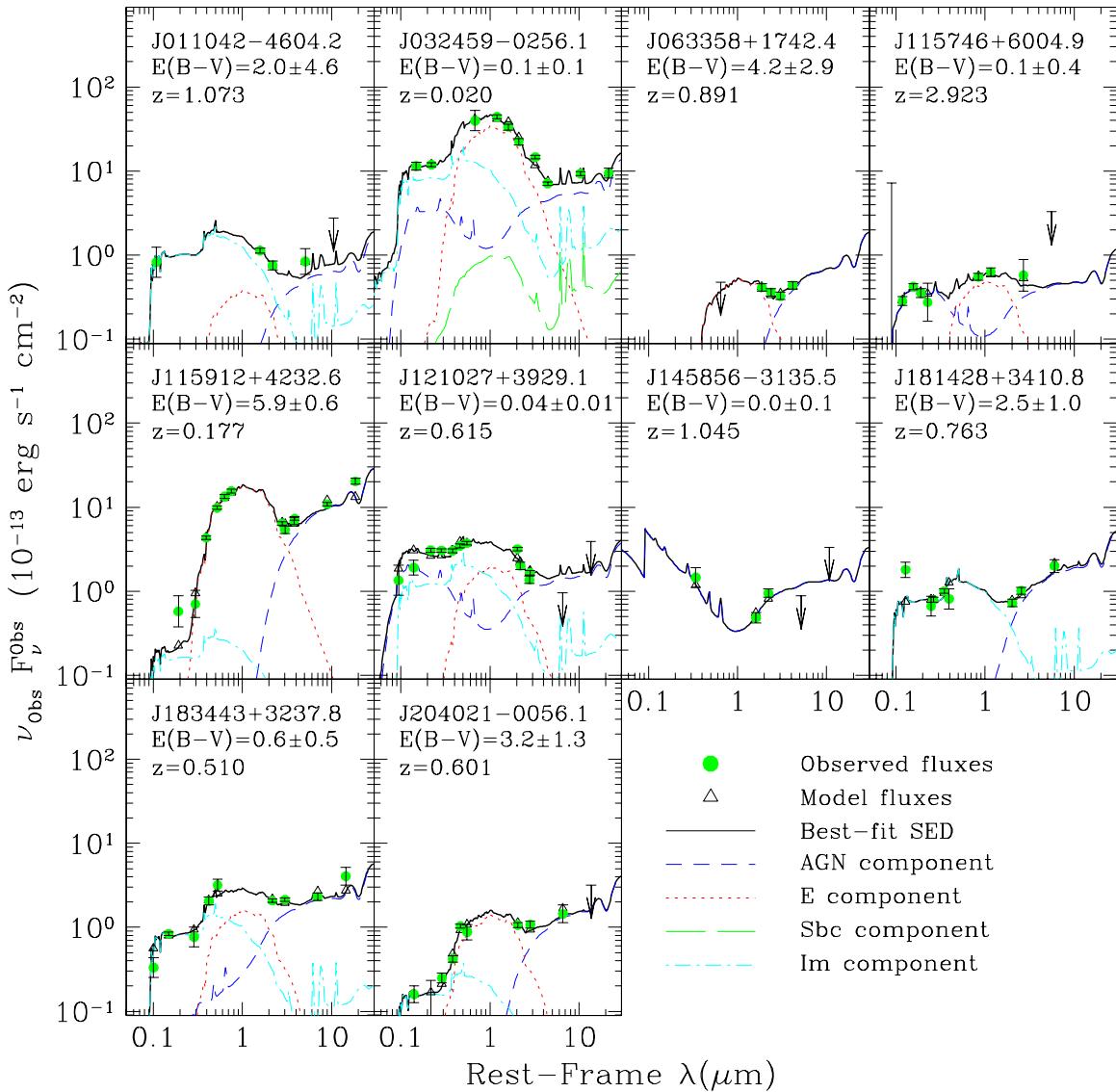
Figure 5. Broad-band UV–MIR SED and best-fitting model solution for the serendipitous *NuSTAR* sources. The data are fitted with the Assef et al. (2010) AGN (magenta dashed curve) and galaxy (elliptical: red dotted curve; spiral: green long-dashed curve; irregular: cyan dash-dotted curve) templates. The best-fitting solution is plotted as a black solid curve. The source redshift, best-fitting dust-reddening solution ($E(B − V)$), and uncertainties are shown.

(A color version of this figure is available in the online journal.)

Swift-BAT; Tueller et al. 2008, 2010; Baumgartner et al. 2013).

4.1. Basic Source Properties

The 8–24 keV fluxes of the *NuSTAR* sources are up to ≈100 times fainter than sources previously detected at ≳10 keV ($f_{8–24\,keV} ≈ (0.6–5.9) × 10^{−13}$ erg s$^{−1}$ cm$^{−2}$, as compared to $f_{8–20\,keV} ≳ 0.4 × 10^{−11}$ erg s$^{−1}$ cm$^{−2}$; e.g., see Table 2 and the *RXTE* data in Revnivtsev et al. 2004). The *NuSTAR* sources also have fainter optical counterparts and lie at higher redshifts than sources previously detected at ≳10 keV ($R ≈ 16–22$ mag and a median redshift of $z ≈ 0.7$, as compared to $V ≈ 10–16$ mag and a median redshift of $z ≈ 0.03$; see Beckmann et al. 2009; Table 3).

In Figure 6 we plot the rest-frame 10–40 keV luminosity versus redshift of the *NuSTAR* sources and compare them to AGNs detected in the *Swift*-BAT survey (e.g., Burlon et al. 2011). With a median luminosity of $L_{10–40\,keV} ≈ 3 × 10^{44}$ erg s$^{−1}$, the *NuSTAR* sources are more luminous than the vast majority

of the *Swift*-BAT AGNs, where ≈80% have $L_{10–40\,keV} < 10^{44}$ erg s$^{−1}$; the median luminosity of the *Swift*-BAT AGNs is $L_{10–40\,keV} ≈ 3 × 10^{43}$ erg s$^{−1}$. The larger fraction of luminous AGNs detected by *NuSTAR*, in comparison to *Swift*-BAT, is a consequence of the higher sensitivity of *NuSTAR* and two additional factors (1) the strong redshift-dependent evolution of luminous AGNs (e.g., Ueda et al. 2003; Barger et al. 2005; Hasinger et al. 2005; Aird et al. 2010), and (2) the comparatively small cosmological volume in which *NuSTAR* is sensitive to AGNs with $L_{10–40\,keV} < 10^{44}$ erg s$^{−1}$ ($z ≲ 0.2$).

The range of redshifts for the *NuSTAR* sources is large ($z = 0.020–2.923$). At $z = 2.923$, NuSTAR J115746+6004.9 is the highest-redshift AGN detected to date at ≳10 keV that does not appear to be strongly beamed (e.g., Beckmann et al. 2009; Burlon et al. 2011; Malizia et al. 2012). By comparison, NuSTAR J032459-0256.1 has a redshift typical of those of the *Swift*-BAT AGNs ($z = 0.020$) but, with $L_{10–40\,keV} ≈ 5 × 10^{41}$ erg s$^{−1}$, it is ≈30 times less luminous than the faintest *Swift-BAT* AGNs; in Section 4.4 we show that this source is
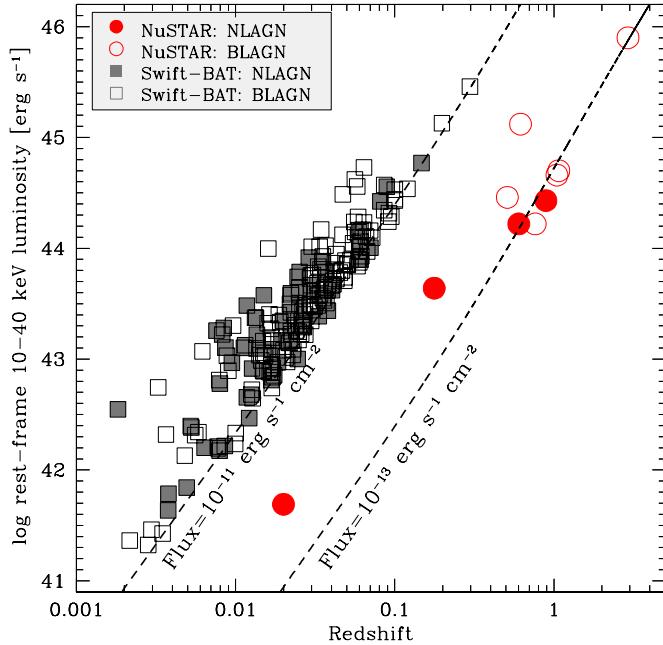
Figure 6. Rest-frame 10–40 keV luminosity vs. redshift for the *NuSTAR* sources (circles) compared to the *Swift*-BAT AGN sample of Burlon et al. (2011; squares); filled symbols indicate narrow-line AGNs (NLAGN) and open symbols indicate broad-line AGNs (BLAGN). The rest-frame 10–40 keV luminosity for the *NuSTAR* sources is calculated directly from the X-ray spectra (see Table 4) while the rest-frame 10–40 keV luminosity for the *Swift*-BAT AGNs is calculated from the observed-frame 15–55 keV flux, assuming $\Gamma = 1.8$ for the *K*-correction factor. The dashed lines indicate different flux limits and show that the *NuSTAR* sources are up to ≈ 100 times fainter than the *Swift*-BAT AGNs.

(A color version of this figure is available in the online journal.)

also unusual since it is hosted in a low-mass dwarf galaxy. The high X-ray luminosities for the majority of the *NuSTAR* sources indicate that they are AGNs. However, the origin of the modest X-ray luminosity of NuSTAR J032459-0256.1 is less clear and it is possible that the X-ray emission is produced by a hyper-luminous X-ray source (HLX; e.g., Farrell et al. 2009; Swartz et al. 2011) as opposed to a low-luminosity AGN; high-spatial resolution observations with *Chandra* would be able to distinguish between an off-nuclear HLX and an AGN or nuclear HLX. The median and range in X-ray luminosity and redshift of the *NuSTAR* sources are consistent with expectations (Ballantyne et al. 2011). However, we note that both the redshift and X-ray luminosity of NuSTAR J032459-0256.1 are below the range typically explored in the models.

The optical spectral properties of the *NuSTAR* sources are relatively diverse; see Figure 3 and Table 3. Five of the ten ($\approx 50^{+34}_{-22}\%$) serendipitous sources have broad emission lines and are classified as BLAGNs, four ($\approx 40^{+32}_{-19}\%$) have narrow emission lines and we classify them as narrow-line AGNs (NLAGNs), and one is a BL Lac object, with strong power-law optical continuum emission and weak emission lines.[31,32] The BL Lac object (NuSTAR J121027+3929.1) is a relatively well studied high-frequency peaked BL Lac object (HBL; Padovani

---

[31] All errors are taken from Tables 1 and 2 of Gehrels (1986) and correspond to the 1σ level; these were calculated assuming Poisson statistics.

[32] We note that our classification of NLAGNs is fairly loose since we lack the emission-line diagnostics around Hα for the majority of our sources to prove that they lie in the AGN region of an emission-line diagnostic diagram as opposed to the H II region (e.g., Baldwin et al. 1981; Veilleux & Osterbrock 1987).

& Giommi 1995), originally identified at X-ray energies by *Einstein* (MS 1207.9+3945; e.g., Gioia et al. 1990; Morris et al. 1991; Urry et al. 2000; Maselli et al. 2008). Two of the NLAGNs have $L_{10-40\,\text{keV}} > 10^{44}$ erg s^{-1} and are therefore type 2 quasars, representing $\approx 20^{+26}_{-13}\%$ of the *NuSTAR* sample; by comparison six type 2 quasars are identified in the 199 *Swift*-BAT sample of Burlon et al. (2011), just $\approx 3^{+2}_{-2}\%$ of the entire sample. However, the difference in the fraction of type 2 quasars between *NuSTAR* and *Swift*-BAT is at least partly related to the increased fraction of luminous AGNs in the *NuSTAR* serendipitous sample; we note that, since we lack coverage of the Hα emission line for the type 2 quasars, we cannot rule out the presence of broad Hα in some of the *NuSTAR* type 2 quasars. The overall fraction of BLAGNs and NLAGNs in the *Swift*-BAT AGN sample is consistent with that found for the *NuSTAR* serendipitous sample: $\approx 50^{+5}_{-5}\%$ of the *Swift*-BAT sources are BLAGNs (including all Seyfert 1s and Seyfert 1.2s) and $\approx 50^{+5}_{-5}\%$ are NLAGNs (including all Seyfert 1.5s, Seyfert 1.8s, Seyfert 1.9s, and Seyfert 2s). Therefore, within the limitations of our small sample, the biggest differences between the basic properties of the *NuSTAR* sources and the *Swift*-BAT AGNs appear to be luminosity and redshift.

4.2. X-Ray Spectral Properties: The Presence of Absorption

The $\gtrsim 10$ keV sensitivity of *NuSTAR* allows for the selection of AGNs almost irrespective of the presence of absorption, up to high absorbing column densities of $N_{\text{H}} \approx (1-3) \times 10^{24}$ cm^{-2}. However, particularly when using lower-energy X-ray data, we can measure the absorbing column densities of the *NuSTAR* sources using the X-ray band ratio (the 8–24 keV to 3–8 keV count-rate ratio) and from fitting the X-ray spectra over a broad energy range.

In Figure 7 we show the X-ray band ratio versus redshift for the *NuSTAR* sources and compare them with those expected for absorbed power-law emission from an AGN. As can be seen, given the high X-ray energies probed by *NuSTAR*, the evidence for absorption can only be clearly identified on the basis of the X-ray band ratio for the most heavily obscured AGNs ($N_{\text{H}} \gtrsim 5 \times 10^{23}$ cm^{-2}) at $z \lesssim 0.5$. The X-ray band ratios for all of the *NuSTAR* sources are consistent with $N_{\text{H}} \lesssim 5 \times 10^{23}$ cm^{-2}. However, more detailed constraints on the X-ray spectral properties and the presence of absorption can be placed by directly fitting the X-ray spectra of the *NuSTAR* sources, particularly when including lower-energy data ($\lesssim 3$ keV), which are more sensitive to column densities of $N_{\text{H}} \lesssim 10^{23}$ cm^{-2}. We extracted the X-ray spectral products and fitted the X-ray data of the *NuSTAR* sources with an absorbed power-law model (ZWABS*POW in XSPEC), following Section 3.1; see Footnote 30 for caveats on the application of an absorbed power-law model to characterize AGNs. In Figure 8 we plot the best-fitting X-ray spectral slope (Γ) and absorbing column density (N_{H}) for the *NuSTAR* sources (see Table 4 for the best-fitting parameters) and compare them to the X-ray spectral properties of the *Swift*-BAT-detected AGNs in Burlon et al. (2011). The best-fitting X-ray spectral slopes of the *NuSTAR* sources are broadly consistent with those found for well-studied nearby AGNs ($\Gamma \approx 1.3-2.3$; e.g., Nandra & Pounds 1994; Reeves & Turner 2000; Deluit & Courvoisier 2003; Piconcelli et al. 2005; Burlon et al. 2011). The source with the steepest X-ray spectral slope ($\Gamma = 2.41^{+0.15}_{-0.14}$) is NuSTAR J121027+3929.1, the HBL previously identified at <10 keV (e.g., Gioia et al. 1990; Morris et al. 1991). Indeed, steep X-ray spectral slopes are typical of HBLs (e.g., Sambruna et al. 1996; Fossati et al. 1997).

Figure 7. X-ray band ratio vs. redshift for the *NuSTAR* sources; see Figure 6 for a description of the symbols. The error bars indicate the 1σ uncertainty on the band ratio, which is calculated following the "numerical method" in Section 1.7.3 of Lyons (1991). The shaded regions show the range of expected band ratios for AGNs with $N_H < 10^{23}$ cm^{-2} and $N_H \approx 5 \times 10^{23}$ cm^{-2}, for an intrinsic spectral slope of $\Gamma = 1.8 \pm 0.5$; the dotted and solid curves indicate the maximum extents in band ratio for $N_H < 10^{23}$ cm^{-2} and $N_H = 5 \times 10^{23}$ cm^{-2}, respectively. The predicted band ratios were calculated using the RMF and ARF for NuSTAR J183443+3237.8 (see Section 2.1.5).

(A color version of this figure is available in the online journal.)
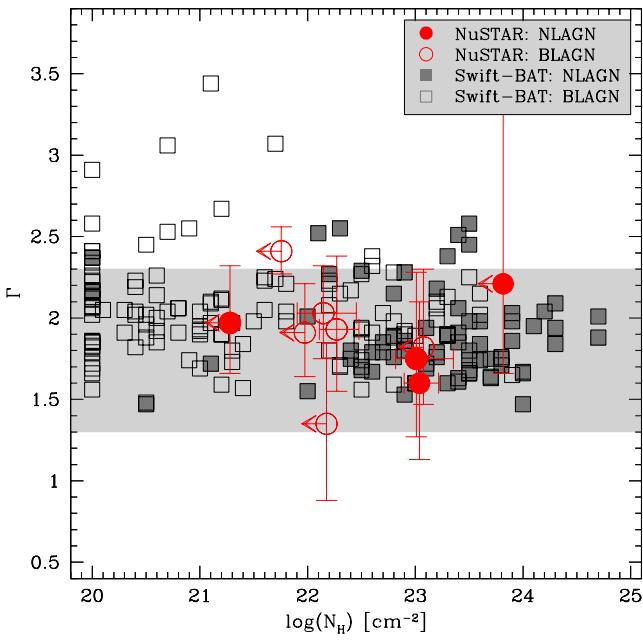
Figure 8. Best-fitting X-ray spectral parameters (Γ vs. N_H) for the *NuSTAR* sources and the *Swift*-BAT AGNs in Burlon et al. (2011). See Figure 6 for a description of the symbols; the error bars indicate 90% confidence uncertainties for one interesting parameter. The shaded region indicates the range of properties found for local AGNs (see Section 4.2).

(A color version of this figure is available in the online journal.)

Four of the ten sources ($\approx 40^{+32}_{-19}\%$) require the presence of absorption, with $N_H \gtrsim 10^{22}$ cm^{-2}, and the other six sources have absorbing column density upper limits. The fraction of X-ray absorbed AGNs with $N_H > 10^{22}$ cm^{-2} in the *Swift*-BAT sample
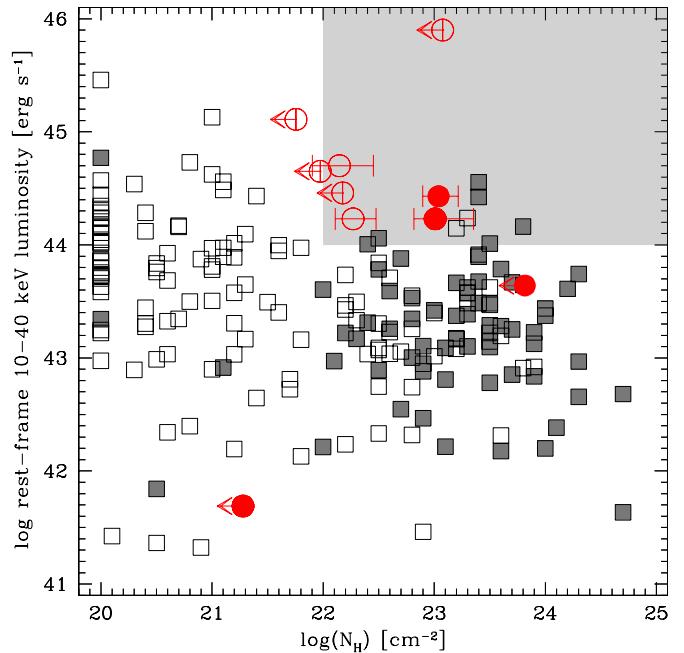
Figure 9. Luminosity vs. best-fitting absorbing column density (N_H) for the *NuSTAR*-detected sources and the *Swift*-BAT AGNs in Burlon et al. (2011). See Figure 6 for a description of the symbols; the error bars indicate 90% confidence uncertainties for one interesting parameter. The shaded region indicates the source properties expected for obscured quasars ($L_{10-40\,keV} \gtrsim 10^{44}$ erg s^{-1} and $N_H \gtrsim 10^{22}$ cm^{-2}).

(A color version of this figure is available in the online journal.)

of Burlon et al. (2011) is $\approx 53^{+4}_{-4}\%$, indicating no significant difference in the fraction of absorbed AGNs between the *NuSTAR* sources and the *Swift*-BAT AGNs. Eight of the *NuSTAR* sources are quasars with $L_{10-40\,keV} > 10^{44}$ erg s^{-1}, and four ($\approx 50^{+40}_{-24}\%$) of the quasars are absorbed with $N_H \gtrsim 10^{22}$ cm^{-2}; see Figure 9. The fraction of obscured quasars is in broad agreement with that found at $\gtrsim 10$ keV in the local universe and from *Chandra* and *XMM-Newton* surveys at higher redshift (e.g., Ueda et al. 2003; La Franca et al. 2005; Akylas et al. 2006; Hasinger 2008; Burlon et al. 2011; Malizia et al. 2012); however, better source statistics are required to provide sufficient constraints to distinguish between different X-ray background synthesis models (Gilli et al. 2007). Two of the X-ray absorbed quasars are BLAGNs and two are NLAGNs and we discuss the origin of the obscuration toward these sources in Section 4.4.

None of the *NuSTAR* sources appear to be absorbed by Compton-thick material ($N_H \gtrsim 10^{24}$ cm^{-2}), despite the near obscuration-independent AGN selection over the *NuSTAR* energy range. However, the absorbing column densities of Compton-thick AGNs are so high that even the >10 keV emission can be significantly absorbed (e.g., AGNs with $N_H \gtrsim 5 \times 10^{24}$ cm^{-2} can be suppressed by an order of magnitude; see Figure 11 of Burlon et al. 2011). Therefore, Compton-thick AGNs can be comparatively rare even in high-energy AGN samples.[33] Indeed, on the basis of the results obtained for local AGNs at >10 keV with the *International Gamma-Ray Astrophysics Laboratory* and *Swift*-BAT observatories, only $\approx 5\%$–10% of the detected sources are Compton-thick AGNs (e.g., Tueller et al. 2008; Beckmann et al. 2009; Burlon et al. 2011; Ajello et al.

---

[33] Less direct approaches are often required to identify Compton-thick AGNs with $N_H \gtrsim 3 \times 10^{24}$ cm^{-2} (e.g., optical–mid-infrared spectroscopy, photometry, and SED fitting; Risaliti et al. 1999; Alexander et al. 2008; Treister et al. 2009a; Goulding et al. 2011; Del Moro et al. 2013; Luo et al. 2013).

2012), despite the intrinsic fraction of Compton-thick AGNs likely being substantially larger.[34] If distant AGNs have a similar range of absorbing column densities as those found locally, we would therefore expect ≈ 0.5–1 Compton-thick AGNs in our small sample; given the tentative evidence for an increase in the fraction of obscured AGNs with redshift (e.g., La Franca et al. 2005; Ballantyne et al. 2006; Treister & Urry 2006; Brightman & Ueda 2012), we may expect the Compton-thick AGN fraction to be even larger in the distant universe. Taking account of the low number statistics of our sample, we can therefore place an upper limit on the fraction of Compton-thick AGNs of $\lesssim 23\%$ in our sample (90% confidence; see Table 1 of Gehrels 1986). The 90% upper limit on the fraction of Compton-thick quasars over the redshift range of $z = 0.5$–1.1 is $\lesssim 33\%$ if we only consider the seven *NuSTAR* sources with $L_{10-40\,keV} > 10^{44}$ erg s^{-1}. These upper limits are marginally too high to distinguish between different model predictions for the fraction of Compton-thick AGNs detected in *NuSTAR* surveys for a range of AGN luminosity functions and column-density distributions ($\lesssim 22\%$; Ballantyne et al. 2011; Akylas et al. 2012). Better source statistics are clearly required to accurately measure the fraction of distant Compton-thick AGNs.

4.3. X-Ray Spectral Properties: The Presence of Reflection

A unique aspect of the *NuSTAR* data is the insight that it places on the >10 keV emission from distant AGNs and the presence of spectral complexity beyond that of simple power-law emission (e.g., a reflection component), particularly at $z \lesssim 1$ where the rest-frame energy coverage of *Chandra* and *XMM-Newton* is comparatively modest. By focusing on >10 keV emission, the effect of absorption on the observed emission will be negligible (at least up to $N_H \approx 5 \times 10^{23}$ cm^{-2}) and the presence of reflection can be revealed by the flattening of the intrinsic power-law component.

To investigate the >10 keV emission in our sources we fitted the rest-frame 10–40 keV emission using a simple power-law model (the POW model in XSPEC), following Section 3.1; see Table 4. The spectral constraints for individual sources are poor and range from $\Gamma_{10-40\,keV} \approx 0.4$–2.4, with large uncertainties; the mean X-ray spectral slope is $\Gamma_{10-40\,keV} \approx 1.9$. However, we can place accurate average spectral constraints by jointly fitting the data. When jointly fitting the data we fitted the rest-frame 10–40 keV data of the *NuSTAR* sources with a power-law model, jointly fitting the power-law component but leaving the normalization for each source to vary independently. In this analysis we excluded NuSTAR J121027+3929.1, the HBL, and NuSTAR J032459-0256.1, the low-luminosity system, since we wanted to focus on luminous non-beamed AGNs. The best-fitting X-ray spectral slope from the joint spectral fitting is $\Gamma_{10-40\,keV} = 1.88^{+0.26}_{-0.25}$, in good agreement with the intrinsic X-ray spectral slope found for nearby AGNs studied at >10 keV (e.g., Deluit & Courvoisier 2003; Dadina 2008; Molina et al. 2009; Burlon et al. 2011); see Table 5. To first order, the comparatively steep average rest-frame 10–40 keV spectral slope suggests that there is not a significant reflection component in these sources, on average, which would manifest itself as a relatively flat X-ray spectral slope at >10 keV (e.g., Nandra & Pounds 1994).

Table 5
Joint-fitting Model Parameters

Model[a]	Sources[b]	$\Gamma_{10-40\,keV}$[c]	R[d]
POW	8	$1.88^{+0.26}_{-0.25}$	. . .
PEXRAV	8	1.8[e]	< 1.4
PEXRAV	8	$2.08^{+0.25}_{-0.24}$	1.0[e]

Notes.
[a] XSPEC model used in the joint-fitting process.
[b] Number of sources used in the joint-fitting process—the low-luminosity system NuSTAR J032459-0256.1 and the HBL NuSTAR J121027+3929.1 were not included in the joint-fitting process.
[c] Best-fitting spectral slope over the rest-frame 10–40 keV range.
[d] Best-fitting reflection parameter (R; see Footnote 36 for a description) over the rest-frame 10–40 keV range.
[e] Parameter fixed at given value.

We can more directly constrain the average strength of the reflection component by jointly fitting the rest-frame 10–40 keV data using the PEXRAV model in XSPEC (Magdziarz & Zdziarski 1995).[35] Fixing the X-ray spectral slope to $\Gamma = 1.8$ and adopting the default parameters for PEXRAV we constrain the average strength of the reflection for the eight *NuSTAR* sources to be $R < 1.4$.[36] Conversely, if we fix $R = 1$, the typical value found for nearby AGNs selected at >10 keV (e.g., Deluit & Courvoisier 2003; Dadina 2008; Beckmann et al. 2009; Molina et al. 2009), we constrain the intrinsic X-ray spectral slope to be $\Gamma = 2.08^{+0.25}_{-0.24}$, also consistent with that of nearby AGNs; see Table 5. To first order, our results therefore suggest that the strength of reflection in distant luminous AGNs is consistent with that found for local AGNs. However, better source statistics are required to more accurately constrain the strength of a reflection component in distant AGNs and to search for changes in the reflection component within subpopulations (e.g., dividing the samples in terms of luminosity and absorbing column density).

4.4. Ultraviolet–Mid-infrared Source Properties

The UV–MIR data of the *NuSTAR* sources can provide insight into the emission from the AGN and host galaxy and the presence of dust reddening. Below we first explore the MIR colors of the *NuSTAR* sources and we then analyze their UV–MIR SEDs.

4.4.1. Infrared Color Analysis

Various work over the past decade has shown that MIR colors provide a powerful method to robustly select luminous AGNs in a manner that is relatively unbiased by obscuration (e.g., Stern et al. 2005, 2012; Assef et al. 2010, 2013; Donley et al. 2007, 2012). As such, MIR selection has some similarity to hard X-ray selection, and MIR and hard X-ray source selection are potentially the two most promising avenues for uncovering the full census of AGNs in the universe. Each wavelength has various strengths and weaknesses. In particular, various work has shown that MIR selection preferentially identifies the most luminous AGN with quasar-level luminosities (e.g., Donley

---

[34] Assuming that the intrinsic distribution of absorbing column densities over $N_H = 10^{22}$–10^{26} cm^{-2} is flat (e.g., Risaliti et al. 1999) and that >10 keV surveys are only sensitive to the identification of AGNs with $N_H \lesssim 3 \times 10^{24}$ cm^{-2}, the intrinsic fraction of Compton-thick AGNs would be $\approx 20\%$–40%.

[35] The PEXRAV model calculates the expected X-ray continuum spectrum due to the reflection of power-law emission by neutral material.
[36] The reflection parameter R indicates the solid angle of a neutral slab of material illuminated by the primary X-ray source: $R \approx \Omega/2\pi$.

et al. 2007; Eckart et al. 2010), while X-ray selection efficiently identifies moderate–high-luminosity AGNs (e.g., Barger et al. 2003; Szokoly et al. 2004; Xue et al. 2011). On the other hand, MIR surveys have now mapped the entire celestial sphere, identifying millions of robust AGN candidates. In contrast, *NuSTAR* is unlikely to map more than ≈ 10–20 deg^2 over its entire mission lifetime. In order to explore this MIR–X-ray complementarity in the new regime offered by *NuSTAR*, we therefore briefly discuss the MIR colors of the 10 serendipitous *NuSTAR* sources.

Only one of the 10 *NuSTAR* sources (NuSTAR J063358+1742.4) has four-band *Spitzer*-IRAC detections, a requirement for the *Spitzer* MIR AGN selection criteria; NuSTAR J063358+1742.4 is fainter than the *WISE* flux limits but has IRAC colors that place it within the IRAC AGN wedge of Stern et al. (2005). Of the other nine *NuSTAR* sources, eight have at least two-band detections by *WISE*. Stern et al. (2012) and Assef et al. (2013) have recently developed *WISE* AGN selection criteria, effectively extending the *Spitzer* selection criteria across the full sky (see also Mateos et al. 2012; Wu et al. 2012). Five of the eight *NuSTAR* sources have *WISE* colors indicative of an AGN according to those criteria. The outliers include the two sources with the weakest AGN component (i.e., lowest $\hat{a}$ values; see Section 3.2), NuSTAR J011042-4604.2 and NuSTAR JJ032459-0256.1. These are the only sources with $\hat{a} < 0.5$, confirming that MIR selection misses sources where the AGN is not bolometrically dominant.

The final outlier is the HBL NuSTAR J121027+3929.1, a BL Lac-type blazar. Massaro et al. (2011) have recently published a series of papers discussing the *WISE* colors of blazars. While flat-spectrum radio quasar type blazars have colors typical of other AGN populations (e.g., Yan et al. 2013), BL Lac-type blazars have unique colors. However, as NuSTAR J121027+3929.1 is only detected in the two shorter wavelength bandpasses of *WISE*, it is not possible to compare this source to the color criteria developed by Massaro et al. (2011) and Yan et al. (2013); note also the caveat in Footnote 3 of Stern & Assef (2013).

4.4.2. Spectral Energy Distribution Analysis

To quantify the UV–MIR emission of the *NuSTAR* sources we fitted the broad-band SEDs following Section 3.2; see Figure 5 and Table 3. A significant AGN component ($\hat{a} > 0.4$) is required to explain the UV–MIR emission for all of the sources except for the low-luminosity system NuSTAR J032459-0256.1. The rest-frame $6\,\mu$m luminosities of the *NuSTAR* sources ($\nu L_{6\,\mu m} \approx (0.9$–$30) \times 10^{44}$ erg s^{-1}, with the exception of NuSTAR J032459-0256.1, which has $\nu L_{6\,\mu m} \approx 4 \times 10^{40}$ erg s^{-1}) are in general agreement with that expected for the MIR–X-ray (i.e., $6\,\mu$m–2–10 keV) luminosity relationship found for AGNs (e.g., Lutz et al. 2004; Fiore et al. 2009); we assumed $\Gamma = 1.8$ to convert between rest-frame 2–10 keV and rest-frame 10–40 keV. However, we note that the HBL NuSTAR J121027+3929.1 and the highest-redshift source NuSTAR J115746+6004.9 are both X-ray bright compared to the strength of the AGN at $6\,\mu$m, suggesting that the X-ray emission from these sources is probably beamed (as would be, at least, expected for an HBL).

In some cases the presence of dust reddening in the best-fitting SED solutions means that the observed contribution of the AGN at UV–optical wavelengths is negligible. However, we highlight here that, although the strength of the AGN continuum at UV–optical wavelengths plotted in Figure 5 is inconsistent with the optical spectroscopy in some cases (e.g.,
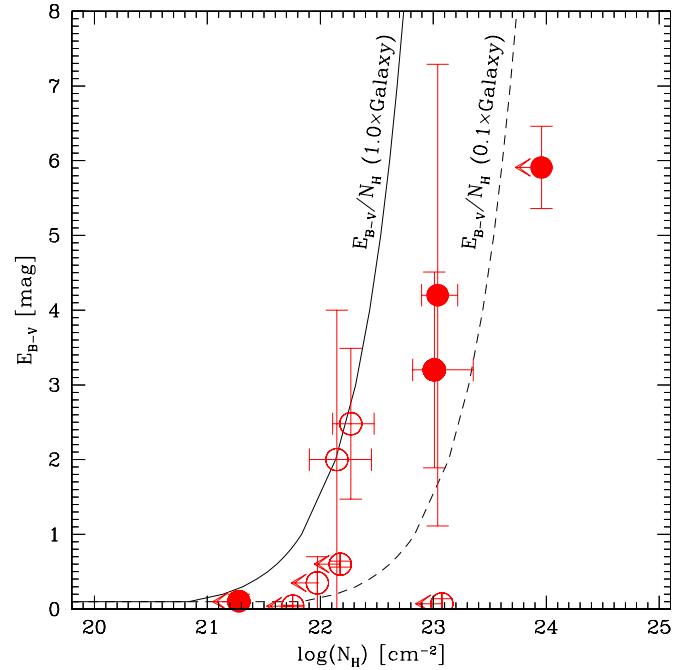

Figure 10. Dust reddening ($E(B - V)$) vs. X-ray absorption (N_H) for the *NuSTAR* serendipitous sources from the UV–MIR SED fitting and the X-ray spectral fitting, respectively; see Figure 6 for the description of the symbols. The solid curve indicates the relationship between dust reddening and X-ray absorption expected from the $A_{V,Gal}$–$N_{H,Gal}$ relationship found in the Galaxy (Savage & Mathis 1979; Güver & Özel 2009) while the dashed curve indicates $A_{V,Gal}$–$10 \times N_{H,Gal}$, broadly consistent with that found for AGNs by Maiolino et al. (2001).

(A color version of this figure is available in the online journal.)

NuSTAR J011042-4604.2 and NuSTAR J181428+3410.8), they are broadly consistent when the range in dust reddening from the best-fitting solution is taken into account; see Table 3. As expected on the basis of the simplest unified AGN model (e.g., Antonucci 1993), the optical emission is heavily extinguished in the NLAGNs ($E(B - V) \approx 3$–6 mag, which corresponds to $A_V \approx 9$–18 mag for $R_V = 3.1$; e.g., Savage & Mathis 1979), with the exception of the low-luminosity system NuSTAR J032459-0256.1. There is evidence of dust reddening for two of the BLAGNs (NuSTAR J181428+3410.8 has $E(B - V) \approx 2$ mag and NuSTAR J183443+3237.8 has $E(B - V) \approx 0.6$ mag) and, as we discuss in the Appendix, the reddening toward NuSTAR J183443+3237.8 appears to be variable. None of the other BLAGNs show evidence for significant obscuration at optical wavelengths, as expected for the simplest version of the unified AGN model for BLAGNs; however, we note that there is a large uncertainty in the dust reddening for NuSTAR J011042-4604.2, which is due to the limited number of photometric data points.

In Figure 10 we compare the obscuration estimated from the UV–MIR SED fitting to that measured from the X-ray spectral fitting, which provides constraints on the dust-to-gas ratio in AGNs. The BLAGN with the strongest dust reddening (NuSTAR J181428+3410.8) has a measured X-ray absorbing column density of $N_H \approx 10^{22}$ cm^{-2}, consistent with that expected given the A_V–N_H relationship found in the Galaxy (e.g., Güver & Özel 2009). The constraints on the X-ray absorbing column density for the other four BLAGNs are also consistent with that expected given the A_V–N_H relationship found in the Galaxy; however, in all cases the column-density constraints are too weak to rule out the different A_V–N_H

relationship found by Maiolino et al. (2001). By comparison, although the three NLAGNs with $L_{10-40\,\mathrm{keV}} \gtrsim 10^{43}$ erg s^{-1} (NuSTAR J063358+1742.4, NuSTAR J115912+4232.6, and NuSTAR J204021-0056.1) have evidence for significant obscuration, the inferred X-ray absorbing column densities from the dust reddening measurements are lower than those directly measured from the X-ray spectral analyses ($N_{\mathrm{H},A_{\mathrm{V}}} \approx (2-4) \times 10^{22}$ cm^{-2}, as compared to $N_{\mathrm{H}} \approx 10^{23}$ cm^{-2} measured from the X-ray data). However, the dust-to-gas ratios are consistent with the lower A_{V}–N_{H} relationship found by Maiolino et al. (2001) for AGNs. Neither the HBL NuSTAR J121027+3929.1 nor the low-luminosity system NuSTAR J032459-0256.1 shows evidence for significant obscuration in the UV–MIR and X-ray bands.

The best-fitting SED solutions also provide a first-order estimate of the host-galaxy stellar masses of the *NuSTAR* sources. The range of stellar masses is large, from $\approx 2 \times 10^9\,M_\odot$ (for the low-luminosity system NuSTAR J032459-0256.1) to $\approx 3 \times 10^{12}\,M_\odot$ (for the highest-redshift source NuSTAR J115746+6004.9). However, the stellar masses for the majority of the *NuSTAR* sources are relatively tightly constrained: the stellar-mass range with these two extreme sources removed is $(0.7-3.3) \times 10^{11}\,M_\odot$, and the median stellar mass is $\approx 10^{11}\,M_\odot$. Many of the *NuSTAR* sources are BLAGNs and we caution that reliable stellar-mass constraints are challenging for these systems due to the contribution of the AGN to the rest-frame optical–near-IR emission (see Section 3.2 and Figure 5 for the SED-fitting constraints). However, reassuringly, the median stellar mass of the NLAGNs, where accurate stellar-mass constraints are less challenging, is consistent with that of the BLAGNs when the two extreme sources are removed ($\approx 10^{11}\,M_\odot$).

The range and median stellar mass of the *NuSTAR* sources are similar to those of comparably distant AGNs detected at <10 keV in *Chandra* and *XMM-Newton* surveys (e.g., Babić et al. 2007; Alonso-Herrero et al. 2008; Bundy et al. 2008; Xue et al. 2010; Lusso et al. 2011). However, by comparison, the median stellar mass of the *NuSTAR* sources is ≈ 5 times higher than for $z < 0.05$ AGNs detected at >10 keV by *Swift*-BAT ($\approx 2 \times 10^{10}\,M_\odot$; Koss et al. 2011). To first order this suggests that there has been significant evolution in the characteristic mass of high-energy emitting AGNs over the redshift range $z \approx 0-1$. However, the *NuSTAR* sources are more luminous than the *Swift*-BAT AGNs and that could bias the results toward more massive systems. For example, for a constant average Eddington ratio, the order of magnitude higher median X-ray luminosity of the *NuSTAR* sources over the *Swift*-BAT AGNs (see Section 4.1) would lead to an order of magnitude higher black-hole mass and thereby a larger stellar mass, assuming no evolution in the black-hole–spheroid mass relationship (e.g., Magorrian et al. 1998; Marconi & Hunt 2003; Gültekin et al. 2009). Indeed, Koss et al. (2011) show a weak trend between mean stellar mass and X-ray luminosity for the *Swift*-BAT AGNs. Therefore, while our results indicate that the most luminous high-energy emitting AGNs at $z \gtrsim 0.1$ are hosted by more massive galaxies than high-energy emitting AGNs at $z < 0.05$, a systematic analysis of both local and distant AGNs taking account of potential X-ray luminosity biases, is required to derive more accurate constraints.

5. CONCLUSIONS

We have reported on the first 10 identifications of *NuSTAR* sources serendipitously detected in the extragalactic survey program. These *NuSTAR* sources are ≈ 100 times fainter than AGNs previously detected at >10 keV and have a broad range in redshift and luminosity ($z = 0.020-2.923$ and $L_{10-40\,\mathrm{keV}} \approx 4 \times 10^{41}-5 \times 10^{45}$ erg s^{-1}); the median redshift and luminosity are $z \approx 0.7$ and $L_{10-40\,\mathrm{keV}} \approx 3 \times 10^{44}$ erg s^{-1}, respectively. On the basis of broad-band $\approx 0.5-32$ keV spectroscopy, optical spectroscopy, and broad-band UV–MIR SED analyses we found the following results.

1. Five ($\approx 50^{+34}_{-22}$%) of the ten *NuSTAR* sources are classified as BLAGNs, four ($\approx 40^{+32}_{-19}$%) are classified as NLAGNs, and one is a BL Lac object. The BLAGN:NLAGN ratio is consistent with that found for $\gtrsim 10$ keV selected AGNs in the local universe. See Section 4.1.

2. From fitting the broad-band X-ray spectra we find that the dominant source population are quasars with $L_{10-40\,\mathrm{keV}} > 10^{44}$ erg s^{-1}, of which ≈ 50% are obscured with $N_{\mathrm{H}} \gtrsim 10^{22}$ cm^{-2}. However, none of the seven quasars over the redshift range $z = 0.5-1.1$ are Compton thick and we place a 90% confidence upper limit of $\lesssim 33$% on the Compton-thick quasar fraction. See Section 4.2.

3. From jointly fitting the rest-frame $\approx 10-40$ keV data for all of the non-beamed sources with $L_{10-40\,\mathrm{keV}} > 10^{43}$ erg s^{-1} we constrain the high-energy X-ray spectral slope and the average strength of a reflection component. We find $R < 1.4$ for $\Gamma = 1.8$ and $\Gamma = 2.08^{+0.25}_{-0.24}$ for $R = 1.0$, consistent with that found for local AGNs selected at >10 keV. See Section 4.3.

4. From fitting the UV–MIR SEDs we constrain the stellar masses of the host galaxies, finding a median stellar mass of $\approx 10^{11}\,M_\odot$. The host galaxies of *NuSTAR* sources are ≈ 5 times more massive on average than *Swift*-BAT-detected local AGNs at >10 keV. At least part of this implied evolution in the characteristic mass of high-energy emitting AGNs is likely to be due to X-ray luminosity biases. See Section 4.4.

NuSTAR is providing unique insight into the high-energy properties of AGNs, achieving a factor ≈ 100 times improvement in sensitivity over previous observatories at $\gtrsim 10$ keV. In the current study we do not find significant differences in the fraction of absorbed AGNs between the *NuSTAR* sources and nearby high-energy emitting AGNs, despite the *NuSTAR* sources being ≈ 10 times more luminous (and ≈ 5 times more massive), on average. These results therefore suggest that the central engine of distant high-energy emitting AGNs is similar to that of nearby AGNs. However, the current study is limited in source statistics and provides a first look at the high-energy properties of distant AGNs. With the $\approx 20-40$ times improvement in sample size afford by the full *NuSTAR* extragalactic survey (completed in the first two years of *NuSTAR* observations) we will be able to make more detailed comparisons and accurately measure the high-energy properties of distant AGNs and constrain their evolution with redshift.
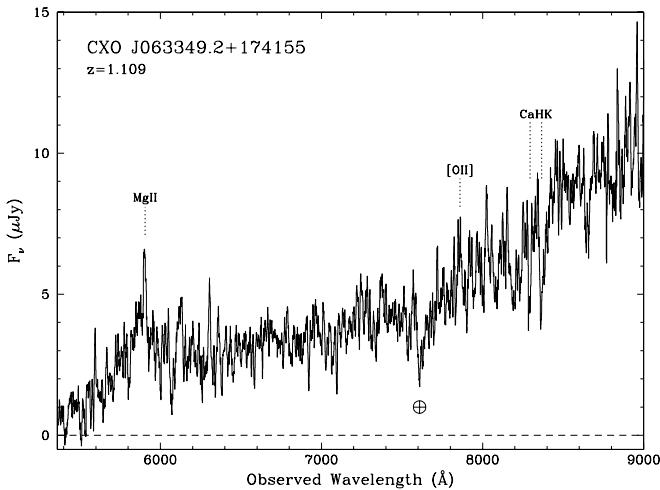
Figure 11. Left: optical spectrum of a *Chandra*-detected source spectroscopically identified in the Geminga field. The detection of broad Mg II indicates that this source is a BLAGN at $z = 1.109$; right: UV–MIR SED with the best-fitting solution. The data are fitted with the Assef et al. (2010) AGN (magenta dashed curve) and elliptical galaxy templates (red dotted curve). The best-fitting solution is plotted as a black solid curve. The source redshift, best-fitting dust-reddening solution ($E(B - V)$), and uncertainties are shown.

(A color version of this figure is available in the online journal.)

APPENDIX

Here we provide the details of the new optical spectroscopy obtained for eight of the serendipitous *NuSTAR* sources, present the optical spectroscopy for an additional *Chandra*-detected source in the Geminga field, and discuss the interesting properties of NuSTAR J183443+3237.8.

A.1. Details of the New Optical Spectrsocopic Observations

On UT 2012 October 10 we used the Double Spectrograph (DBSP) on the Palomar 200 inch telescope to observe NuSTAR J183443+3237.8 in the 3C382 field. We integrated for 300 s split across two equal exposures in moderate, but non-photometric conditions. The observations used the 2″0 wide longslit, the 6800 Å dichroic, the 600/4000 blue grating (e.g., $600\,\ell\,mm^{-1}$, blazed at 4000 Å), and the 316/7500 red grating.
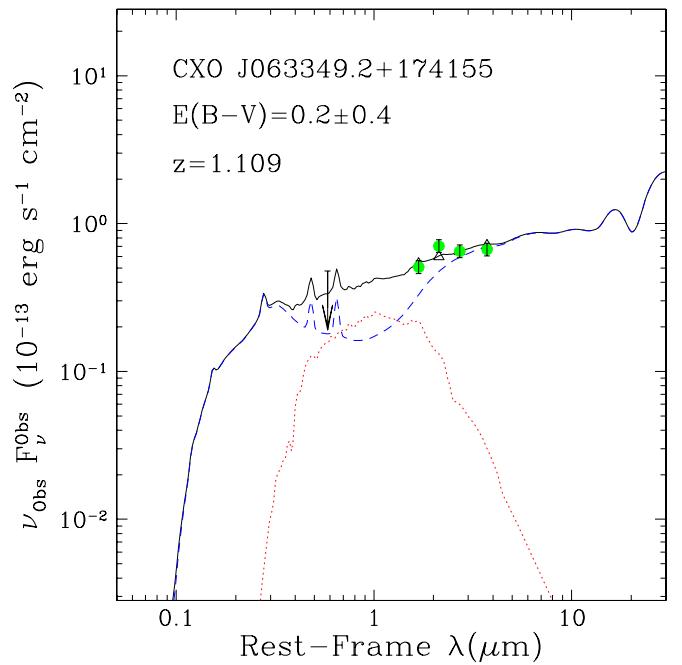
On UT 2012 October 13 we used the DEep Imaging Multi-Object Spectrograph (DEIMOS; Faber et al. 2003) at the Nasymth focus of the Keck II 10 m telescope to observe NuSTAR J204021-0056.1 in the AE Aqr field. We obtained a single 300 s exposure in photometric conditions using 600/7500 grating.

On UT 2012 November 9 we used the Low Resolution Imaging Spectrometer (LRIS; Oke et al. 1995) at the Cassegrain focus of the Keck I telescope to observe NuSTAR J032459-0256.1 and NuSTAR J181428+3410.8 in the NGC 1320 and W1814+3412 fields, respectively. We observed the sources for 200 s and 300 s, respectively, in moderate, but non-photometric conditions. The observations used the 1″5 wide longslit, the 5600 Å dichroic, the 400/3400 blue grism, and the 400/8500 red grating.

On UT 2012 November 20 we again used DBSP at Palomar. Conditions were photometric and we used the same instrument configuration as employed for NuSTAR J183443+3237.8 in October. We observed NuSTAR J115746+6004.9 and NuSTAR J115912+4232.6 in the SDSS 1157+6003 and IC 751 fields for 1800 s split into two and three dithered exposures, respectively.

On UT 2012 December 12 we used the Gemini Multi-Object Spectrograph-South (GMOS-S; Hook et al. 2004) at the Gemini-South 8 m telescope to observe NuSTAR J011042-4604.2 in the HLX 1 field. We observed the source for 1200 s, split into two exposures dithered by 50 Å in central wavelength to fill in the chip gap in the focal plane. We used the 1″5 wide longslit and 600/4610 grating.

On UT 2013 January 10 we used LRIS at the Keck I telescope to observe NuSTAR J063358+1742.4 in the Geminga field. We observed the source for 1200 s, split into two exposures, using the 1″5 wide longslit, the 600/4000 blue grism, the 400/8500 red grating, and the 5600 Å dichroic. The position angle of the longslit was set in order to get a second *Chandra* source in
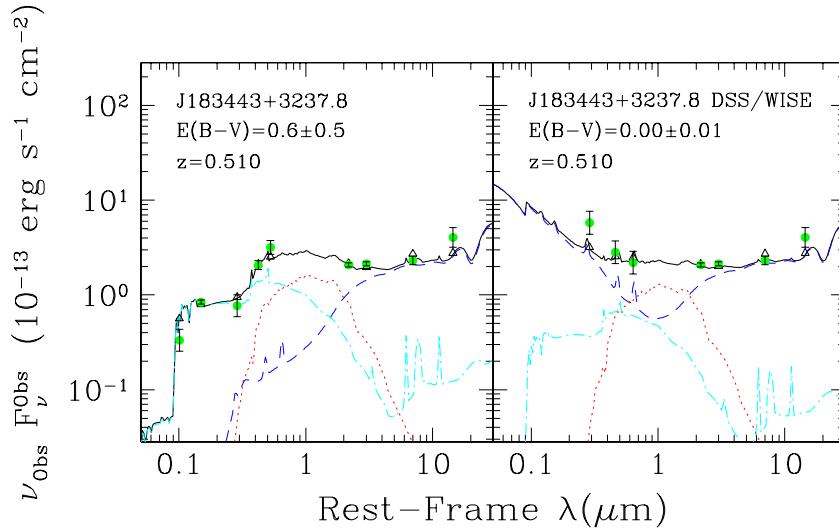
Figure 12. UV–MIR SED and best-fitting solutions for NuSTAR J183443+3237.8 using (left) our recent (UT 2013 March 4) observations and (right) from the DSS. The data are fitted with the Assef et al. (2010) AGN (magenta dashed curve) and galaxy (elliptical: red dotted curve; irregular: cyan dash-dotted curve) templates; the best-fitting solution is plotted as a black solid curve. The source redshift, best-fitting dust-reddening solution ($E(B-V)$) and uncertainties are shown.

(A color version of this figure is available in the online journal.)

the field where there is weak evidence for *NuSTAR* emission. The optical spectrum of this second Geminga serendipitous source at $\alpha_{\rm J2000} = 06^{\rm h}33^{\rm m}49^{\rm s}22$, $\delta_{\rm J2000} = +17°41'55''.1$ (CXO J063349.2+174155) and the UV–MIR SED and the best-fitting solution (following Section 3.2) are shown in Figure 11. The optical spectrum reveals an AGN at $z = 1.109$ with somewhat broadened Mg II emission, weak [O II] emission, and a strong 4000 Å break with well-detected Ca H+K absorption lines. The best-fitting SED solution suggests that the AGN dominates the UV–MIR emission. However, since the SED only comprises the *WISE* data, the overall SED is comparatively poorly constrained: the best-fitting parameters are $\hat{a} = 0.93 \pm 0.03$, $E(B-V) = 0.24 \pm 0.39$, $L_{6\mu m} = (5.34 \pm 0.55) \times 10^{44}$ erg s^{-1}, and $M_* = (9.3 \pm 3.2) \times 10^{10} M_\odot$. There is weak evidence for emission from this source in the *NuSTAR* images. However, this source was not formally detected using the source detection procedure described in Section 2.1 and we therefore do not discuss this source further in this paper. We instead provide this information for future researchers of X-ray sources in the Geminga field.

A.2. Notes on NuSTAR J183443+32378

NuSTAR J183443+3237.8 is a BLAGN that appears to be unabsorbed in the X-ray band ($N_{\rm H} < 1.5 \times 10^{22}$ cm^{-2}; see Table 4). We obtained B-, R-, and I-band observations of this field on UT 2013 March 4 using P60; see Section 2.4. The optical emission of NuSTAR J183443+3237.8 has faded since the original DSS observations. To explore the origin of this fading we fitted the UV–MIR SED of NuSTAR J183443+3237.8 following Section 3.2, using both our new data and the older DSS data; see Figure 12. On the basis of the original DSS observations the best-fitting SED solution indicates $E(B-V) = 0.00 \pm 0.01$. However, by the comparison, the best-fitting SED solution using the new UV–optical data indicates $E(B-V) = 0.59 \pm 0.46$, consistent with $A_{\rm V} \approx 1.9$ mag for $R_{\rm V} = 3.1$ (e.g., Savage & Mathis 1979). Assuming the relationship between dust reddening and X-ray absorption found in the Galaxy (e.g., Güver & Özel 2009), the X-ray absorbing column density for $A_{\rm V} \approx 1.9$ mag is $N_{\rm H} \approx 5 \times 10^{21}$ cm^{-2}, a factor ≈ 3 below the

upper limit placed on $N_{\rm H}$ from the X-ray spectral fitting; see Table 4.

REFERENCES

Aird, J., Nandra, K., Laird, E. S., et al. 2010, MNRAS, 401, 2531
Ajello, M., Alexander, D. M., Greiner, J., et al. 2012, ApJ, 749, 21
Ajello, M., Greiner, J., Kanbach, G., et al. 2008, ApJ, 678, 102
Akylas, A., Georgakakis, A., Georgantopoulos, I., Brightman, M., & Nandra, K. 2012, A&A, 546, A98
Akylas, A., Georgantopoulos, I., Georgakakis, A., Kitsionas, S., & Hatzimi-naoglou, E. 2006, A&A, 459, 693
Alexander, D. M., Bauer, F. E., Brandt, W. N., et al. 2003a, AJ, 126, 539
Alexander, D. M., Bauer, F. E., Brandt, W. N., et al. 2003b, AJ, 125, 383
Alexander, D. M., Chary, R.-R., Pope, A., et al. 2008, ApJ, 687, 835
Alonso-Herrero, A., Pérez-González, P. G., Rieke, G. H., et al. 2008, ApJ, 677, 127
Antonucci, R. 1993, ARA&A, 31, 473
Arnaud, K. A. 1996, in ASP Conf. Ser. 101, Astronomical Data Analysis Software and Systems V, ed. G. H. Jacoby & J. Barnes (San Francisco, CA: ASP), 17
Assef, R. J., Kochanek, C. S., Brodwin, M., et al. 2008, ApJ, 676, 286
Assef, R. J., Kochanek, C. S., Brodwin, M., et al. 2010, ApJ, 713, 970
Assef, R. J., Stern, D., Kochanek, C. S., et al. 2013, ApJ, 772, 26
Avni, Y. 1976, ApJ, 210, 642
Babić, A., Miller, L., Jarvis, M. J., et al. 2007, A&A, 474, 755
Baldwin, J. A., Phillips, M. M., & Terlevich, R. 1981, PASP, 93, 5
Ballantyne, D. R., Draper, A. R., Madsen, K. K., Rigby, J. R., & Treister, E. 2011, ApJ, 736, 56
Ballantyne, D. R., Everett, J. E., & Murray, N. 2006, ApJ, 639, 740
Barger, A. J., Cowie, L. L., Capak, P., et al. 2003, AJ, 126, 632
Barger, A. J., Cowie, L. L., Mushotzky, R. F., et al. 2005, AJ, 129, 578
Bassani, L., Molina, M., Malizia, A., et al. 2006, ApJL, 636, L65
Baumgartner, W. H., Tueller, J., Markwardt, C. B., et al. 2013, ApJS, 207, 19
Becker, R. H., White, R. L., & Helfand, D. J. 1995, ApJ, 450, 559
Beckmann, V., Soldi, S., Ricci, C., et al. 2009, ApJ, 505, 417
Bell, E. F., McIntosh, D. H., Katz, N., & Weinberg, M. D. 2003, ApJS, 149, 289
Bird, A. J., Bazzano, A., Bassani, L., et al. 2010, ApJS, 186, 1
Bottacini, E., Ajello, M., & Greiner, J. 2012, ApJS, 201, 34
Brandt, W. N., & Alexander, D. M. 2010, PNAS, 107, 7184
Brandt, W. N., Alexander, D. M., Hornschemeier, A. E., et al. 2001, AJ, 122, 2810
Brandt, W. N., & Hasinger, G. 2005, ARA&A, 43, 827
Brightman, M., & Ueda, Y. 2012, MNRAS, 423, 702
Brunner, H., Cappelluti, N., Hasinger, G., et al. 2008, A&A, 479, 283
Bundy, K., Georgakakis, A., Nandra, K., et al. 2008, ApJ, 681, 931
Burlon, D., Ajello, M., Greiner, J., et al. 2011, ApJ, 728, 58

Caccianiga, A., Severgnini, P., Della Ceca, R., et al. 2008, A&A, 477, 735
Cash, W. 1979, ApJ, 228, 939
Comastri, A., Ranalli, P., Iwasawa, K., et al. 2011, A&A, 526, L9
Condon, J. J., Cotton, W. D., Greisen, E. W., et al. 1998, AJ, 115, 1693
Dadina, M. 2008, A&A, 485, 417
Del Moro, A., Alexander, D. M., Mullaney, J. R., et al. 2013, A&A, 549, A59
Deluit, S., & Courvoisier, T. J.-L. 2003, A&A, 399, 77
Donley, J. L., Koekemoer, A. M., Brusa, M., et al. 2012, ApJ, 748, 142
Donley, J. L., Rieke, G. H., Pérez-González, P. G., Rigby, J. R., & Alonso-
    Herrero, A. 2007, ApJ, 660, 167
Eckart, M. E., McGreer, I. D., Stern, D., Harrison, F. A., & Helfand, D. J.
    2010, ApJ, 708, 584
Eisenhardt, P. R. M., Wu, J., Tsai, C.-W., et al. 2012, ApJ, 755, 173
Faber, S., Phillips, A. C., Kibrick, R. I., et al. 2003, Proc. SPIE, 4841, 1657
Farrell, S. A., Webb, N. A., Barret, D., Godet, O., & Rodrigues, J. M.
    2009, Natur, 460, 73
Fazio, G. G., Hora, J. L., Allen, L. E., et al. 2004, ApJS, 154, 10
Fiore, F., Puccetti, S., Brusa, M., et al. 2009, ApJ, 693, 447
Fossati, G., Celotti, A., Ghisellini, G., & Maraschi, L. 1997, MNRAS, 289, 136
Freeman, P. E., Kashyap, V., Rosner, R., & Lamb, D. Q. 2002, ApJS, 138, 185
Frontera, F., Orlandini, M., Landi, R., et al. 2007, ApJ, 666, 86
Fruscione, A., McDowell, J. C., Allen, G. E., et al. 2006, Proc. SPIE, 6270,
    62701V
Geach, J. E., Alexander, D. M., Lehmer, B. D., et al. 2009, ApJ, 700, 1
Gehrels, N. 1986, ApJ, 303, 336
Giacconi, R., Gursky, H., Paolini, F. R., & Rossi, B. B. 1962, PhRvL, 9, 439
Gilli, R., Comastri, A., & Hasinger, G. 2007, A&A, 463, 79
Gioia, I. M., Maccacaro, T., Schild, R. E., et al. 1990, ApJS, 72, 567
Goulding, A. D., Alexander, D. M., Mullaney, J. R., et al. 2011, MNRAS,
    411, 1231
Gültekin, K., Richstone, D. O., Gebhardt, K., et al. 2009, ApJ, 698, 198
Güver, T., & Özel, F. 2009, MNRAS, 400, 2050
Hambly, N. C., MacGillivray, H. T., Read, M. A., et al. 2001, MNRAS,
    326, 1279
Harrison, F. A., Craig, W. W., Christensen, F. E., et al. 2013, ApJ, 770, 103
Harrison, F. A., Eckart, M. E., Mao, P. H., Helfand, D. J., & Stern, D. 2003, ApJ,
    596, 944
Hasinger, G. 2008, A&A, 490, 905
Hasinger, G., Cappelluti, N., Brunner, H., et al. 2007, ApJS, 172, 29
Hasinger, G., Miyaji, T., & Schmidt, M. 2005, A&A, 441, 417
Hickox, R. C., & Markevitch, M. 2006, ApJ, 645, 95
Hook, I. M., Jørgensen, I., Allington-Smith, J. R., et al. 2004, PASP, 116, 425
Kim, D.-W., Cameron, R. A., Drake, J. J., et al. 2004, ApJS, 150, 19
Koss, M., Mushotzky, R., Veilleux, S., et al. 2011, ApJ, 739, 57
Krivonos, R., Revnivtsev, M., Lutovinov, A., et al. 2007, A&A, 475, 775
La Franca, F., Fiore, F., Comastri, A., et al. 2005, ApJ, 635, 864
Lehmer, B. D., Brandt, W. N., Alexander, D. M., et al. 2005, ApJS, 161, 21
Lehmer, B. D., Xue, Y. Q., Brandt, W. N., et al. 2012, ApJ, 752, 46
Luo, B., Bauer, F. E., Brandt, W. N., et al. 2008, ApJS, 179, 19
Luo, B., Brandt, W. N., Alexander, D. M., et al. 2013, ApJ, 772, 153
Lusso, E., Comastri, A., Vignali, C., et al. 2011, A&A, 534, A110
Lutz, D., Maiolino, R., Spoon, H. W. W., & Moorwood, A. F. M. 2004, A&A,
    418, 465
Lyons, L. (ed.) 1991, in A Practical Guide to Data Analysis for Physical Science
    Students (Cambridge: Cambridge Univ. Press), 107
Magdziarz, P., & Zdziarski, A. A. 1995, MNRAS, 273, 837
Magorrian, J., Tremaine, S., Richstone, D., et al. 1998, AJ, 115, 2285

Maiolino, R., Marconi, A., Salvati, M., et al. 2001, A&A, 365, 28
Malizia, A., Bassani, L., Bazzano, A., et al. 2012, MNRAS, 426, 1750
Marconi, A., & Hunt, L. K. 2003, ApJL, 589, L21
Markwardt, C. B., Tueller, J., Skinner, G. K., et al. 2005, ApJL, 633, L77
Martin, D. C., Fanson, J., Schiminovich, D., et al. 2005, ApJL, 619, L1
Maselli, A., Giommi, P., Perri, M., et al. 2008, A&A, 479, 35
Massaro, F., D'Abrusco, R., Ajello, M., Grindlay, J. E., & Smith, H. A.
    2011, ApJL, 740, L48
Mateos, S., Alonso-Herrero, A., Carrera, F. J., et al. 2012, MNRAS, 426, 3271
Minkowski, R. L., & Abell, G. O. 1963, in Basic Astronomical Data: Stars and
    Stellar Systems, ed. K. A. Strand (Chicago, IL: Univ. Chicago Press), 481
Molina, M., Bassani, L., Malizia, A., et al. 2009, MNRAS, 399, 1293
Moretti, A., Pagani, C., Cusumano, G., et al. 2009, A&A, 493, 501
Morris, S. L., Stocke, J. T., Gioia, I. M., et al. 1991, ApJ, 380, 49
Nandra, K., & Pounds, K. A. 1994, MNRAS, 268, 405
Nousek, J. A., & Shue, D. R. 1989, ApJ, 342, 1207
Oke, J. B., Cohen, J. G., Carr, M., et al. 1995, PASP, 107, 375
Padovani, P., & Giommi, P. 1995, ApJ, 444, 567
Penzias, A. A., & Wilson, R. W. 1965, ApJ, 142, 419
Piconcelli, E., Jimenez-Bailón, E., Guainazzi, M., et al. 2005, A&A, 432, 15
Reeves, J. N., & Turner, M. J. L. 2000, MNRAS, 316, 234
Reuland, M., van Breugel, W., Röttgering, H., et al. 2003, ApJ, 592, 755
Revnivtsev, M., Sazonov, S., Jahoda, K., & Gilfanov, M. 2004, A&A, 418, 927
Risaliti, G., Maiolino, R., & Salvati, M. 1999, ApJ, 522, 157
Sambruna, R. M., Maraschi, L., & Urry, C. M. 1996, ApJ, 463, 444
Savage, B. D., & Mathis, J. S. 1979, ARA&A, 17, 73
Sazonov, S. Y., & Revnivtsev, M. G. 2004, A&A, 423, 469
Scoville, N., Aussel, H., Brusa, M., et al. 2007, ApJS, 172, 1
Skrutskie, M. F., Cutri, R. M., Stiening, R., et al. 2006, AJ, 131, 1163
Stern, D., & Assef, R. J. 2013, ApJL, 764, L30
Stern, D., Assef, R. J., Benford, D. J., et al. 2012, ApJ, 753, 30
Stern, D., Eisenhardt, P., Gorjian, V., et al. 2005, ApJ, 631, 163
Stocke, J. T., Liebert, J., Schmidt, G., et al. 1985, ApJ, 298, 619
Swartz, D. A., Soria, R., Tennant, A. F., & Yukita, M. 2011, ApJ, 741, 49
Szokoly, G. P., Bergeron, J., Hasinger, G., et al. 2004, ApJS, 155, 271
Treister, E., Cardamone, C. N., Schawinski, K., et al. 2009a, ApJ, 706, 535
Treister, E., & Urry, C. M. 2006, ApJL, 652, L79
Treister, E., Urry, C. M., & Virani, S. 2009b, ApJ, 696, 110
Tueller, J., Baumgartner, W. H., Markwardt, C. B., et al. 2010, ApJS, 186, 378
Tueller, J., Mushotzky, R. F., Barthelmy, S., et al. 2008, ApJ, 681, 113
Ueda, Y., Akiyama, M., Ohta, K., & Miyaji, T. 2003, ApJ, 598, 886
Urry, C. M., Scarpa, R., O'Dowd, M., et al. 2000, ApJ, 532, 816
Vasudevan, R. V., Brandt, W. N., Mushotzky, R. F., et al. 2013, ApJ, 763, 111
Veilleux, S., & Osterbrock, D. E. 1987, ApJS, 63, 295
Watson, M. G., Schröder, A. C., Fyfe, D., et al. 2009, A&A, 493, 339
Winter, L. M., Mushotzky, R. F., Reynolds, C. S., & Tueller, J. 2009, ApJ,
    690, 1322
Worsley, M. A., Fabian, A. C., Bauer, F. E., et al. 2005, MNRAS, 357, 1281
Wright, E. L., Eisenhardt, P. R. M., Mainzer, A. K., et al. 2010, AJ, 140, 1868
Wu, X.-B., Hao, G., Jia, Z., Zhang, Y., & Peng, N. 2012, AJ, 144, 49
Xue, Y. Q., Brandt, W. N., Luo, B., et al. 2010, ApJ, 720, 368
Xue, Y. Q., Luo, B., Brandt, W. N., et al. 2011, ApJS, 195, 10
Xue, Y. Q., Wang, S. X., Brandt, W. N., et al. 2012, ApJ, 758, 129
Yan, L., Donoso, E., Tsai, C.-W., et al. 2013, AJ, 145, 55
Yang, Y., Zabludoff, A., Tremonti, C., Eisenstein, D., & Davé, R. 2009, ApJ,
    693, 1579
York, D. G., Adelman, J., Anderson, J. E., Jr., et al. 2000, AJ, 120, 1579